Validating floc settling velocity models in rivers and freshwater wetlands

Justin A. Nghiem[1], Gen K. Li[1,2], Joshua P. Harringmeyer[3], Gerard Salter[1], Cédric G. Fichot[3], Luca Cortese[3], Michael P. Lamb[1]

5 [1]Division of Geological and Planetary Sciences, California Institute of Technology, Pasadena, 91125, USA
[2]Department of Earth Science, University of California, Santa Barbara, Santa Barbara, 93106, USA
[3]Department of Earth and Environment, Boston University, Boston, 02215, USA

Correspondence to: Justin A. Nghiem (jnghiem@caltech.edu)

Abstract. Flocculation controls mud sedimentation and organic carbon burial rates by increasing mud settling velocity. Floc
10 settling velocity can be predicted using a semi-empirical model that depends on turbulence, sediment concentration, and
geochemical variables or an explicit Stokes law-type model that depends on floc diameter, permeability, and fractal
properties. However, validation of the semi-empirical and explicit models with direct field measurements is lacking. We
employed a camera, in situ particle sizing, and analysis of grain size-specific suspended sediment concentration profiles to
measure flocs in the freshwater channels and wetlands of Wax Lake Delta, Louisiana. Sediment finer than ~20 to 50 μm
15 flocculates with median floc diameter of 30 to 90 μm, bulk solid fraction of 0.05 to 0.3, and floc settling velocity of ~0.1 to 1
mm s^{-1}, with little variation along depth. These values are consistent with the semi-empirical model, which indicates that
turbulence limits variation in floc settling velocity on flood-to-seasonal time scales. In the explicit model, the effective
primary particle diameter, commonly assumed to be the median primary particle diameter, differs by a factor of ~2 to 6
smaller than the median and can be better described using a simple fractal theory. Flow through the floc increases settling
20 velocity by a factor of ~2 and can be explained by parameterizing flocs as effectively permeable clusters of primary
particles. Our results provide the first full field validation of effective primary particle diameter and floc permeability
theories, which improve floc settling velocity predictions of the explicit model.

1 Introduction

Mud, defined as grains with diameter finer than 62.5 μm, constitutes the bulk of sediment load in large alluvial rivers and
25 deltas (Walling and Fang, 2003; Cohen et al., 2022). Mud deposition can counteract land loss in coastal areas experiencing
sea level rise, subsidence, and reduced sediment supply (Blum and Roberts, 2009; Syvitski et al., 2009). Mud also hosts
abundant mineral-bound organic carbon and pollutants, making mud fluxes in rivers relevant to the global carbon cycle
(Mayer, 1994; Galy et al., 2008; Blair and Aller, 2012) and water quality (Nelson and Lamothe, 1993; Pizzuto, 2014).
Understanding mud sedimentation relies on knowledge of flocculation because flocculation can drastically increase the in

30   situ mud settling velocity, affect mud deposition and entrainment fluxes, and ultimately alter mud transport patterns (Lamb et al., 2020; Zeichner et al., 2021).

Flocculation is the reversible process by which individual suspended sediment grains (primary particles) aggregate into larger and less dense particles called flocs, which can settle orders-of-magnitude faster than their primary particles (Chase, 1979; Winterwerp, 1998). Many physical, chemical, and biological mechanisms are known to affect flocculation like

35   turbulence, sediment concentration and mineralogy, organics, and water chemistry (Kranck, 1984; Winterwerp, 1998; Nghiem et al., 2022). In particular, researchers have long studied flocculation in estuaries and the ocean where salinity is a key driver of flocculation (Kranck and Milligan, 1980; McCave, 1984; Hill et al., 2001). However, much less is known about flocs in freshwater environments where organic matter might instead be the main flocculating agent (Eisma et al., 1982; Lee et al., 2019; Zeichner et al., 2021). Limited direct observations have shown that freshwater flocs are ~10 to 100 μm in

40   diameter and settle at ~0.1 to 1 mm s^{-1} (Droppo and Ongley, 1994; Krishnappan, 2000; Guo and He, 2011; Larsen et al., 2009; Osborn et al., 2021). These ranges largely match those measured in estuaries and the ocean (McCave, 1984; Gibbs, 1985) despite the salinity difference. More recent studies analyzed river suspended sediment concentration-depth profiles to infer floc settling velocities and revealed evidence for widespread flocculation of in rivers (Lamb et al., 2020; Nghiem et al., 2022), pointing to the need to calibrate and validate models for riverine flocs.

45   Although floc settling velocity is vital for understanding mud transport in rivers and freshwater wetlands, settling velocity models for freshwater flocs are still in their infancy. Strom and Keyvani (2011) derived a general floc settling velocity model by assuming that flocs are fractal aggregates and modifying the classic Stokes settling velocity model to include floc density and permeability effects. We refer to this modified Stokes model as the "explicit model" because it predicts floc settling velocity from fundamental physical principles. The explicit model can be difficult to use because it

50   requires knowledge of the floc diameter. Alternatively, the floc diameter and settling velocity can be predicted using a flocculation model. In a seminal study, Winterwerp (1998) developed a turbulence-driven model aimed at estuarine flocculation in which the relative rates of floc aggregation (due to particle collisions) and breakage (due to shear stress on flocs) determine the floc diameter, which can be converted to floc settling velocity using a settling velocity model. The Winterwerp model is a function of shear rate and sediment concentration, but is limited because the effects of other factors

55   must be calibrated. Nghiem et al. (2022) modified the Winterwerp model to include dependencies on organic matter, sediment mineralogy, and water chemistry and fitted the model to a global river compilation. We refer to the Nghiem et al. (2022) model as the "semi-empirical model" because it contains fitted parameters that implicitly account for the natural heterogeneity in floc structure, density, and permeability considered in the explicit model.

Both the explicit and semi-empirical models face many uncertainties in practice. The explicit model was validated

60   against a large data compilation of floc diameter and settling velocity measurements (Strom and Keyvani, 2011), but the effects of primary particle diameter and floc permeability remain poorly constrained in general because paired floc diameter and settling velocity measurements alone cannot distinguish between them. The semi-empirical model was calibrated on floc

diameter and settling velocity inferred from river suspended sediment concentration-depth profiles using Rouse-Vanoni theory (Nghiem et al., 2022) and has yet to be verified against direct floc measurements.

65   Here, we combined geochemical sampling, camera observations, in situ laser diffraction particle sizing, and Rouse-Vanoni analysis of suspended sediment concentration-depth profiles in the freshwater Wax Lake Delta (WLD), Louisiana, USA to characterize flocs and examine these knowledge gaps. First, we present a detailed review of the floc theory that we aim to test (Sect. 2). We introduce the study area in Sect. 3. Next, we describe the field methods and data analysis to calculate the floc properties to compare to theory (Sect. 4). Section 5 reports the results and theory comparison including floc

70   fractal dimension, permeability, primary particle diameter, floc size and settling velocity distributions, and semi-empirical model predictions of floc settling velocity. In Sect. 6, we discuss the practical considerations for predicting freshwater floc settling velocity, the physical interpretation of primary particle and permeability effects on floc settling velocity, and the role of environmental feedbacks in determining floc settling velocity in natural settings.

2 Floc Theory

75   We evaluated two complementary approaches, the explicit and semi-empirical models, to predict floc settling velocity, w_s (m s^{-1}).

2.1 Explicit Model

The explicit model is Stokes law modified for flocs (Strom and Keyvani, 2011):

$$w_s = \frac{R_s g D_p^2}{b_1 \Omega v} \left(\frac{D_f}{D_p}\right)^{n_f - 1} ,$$ (1)

80   where R_s is the submerged specific gravity of sediment (= 1.65), g is gravitational acceleration (= 9.81 m s^{-2}), D_p (m) is the effective primary particle diameter, and b_1 (dimensionless) is assumed to be 20 (Ferguson and Church, 2004). The drag ratio, $\Omega \in (0, 1]$ (dimensionless), is the ratio of the drag force of the floc and that of an impermeable particle with the same density and diameter at the same flow velocity (Neale et al., 1973). Equivalently, Ω is the ratio of the settling velocity of the impermeable particle and that of the floc. If $\Omega < 1$, then through-flow in the floc reduces the drag coefficient and increases

85   the settling velocity relative to those of the equivalent impermeable particle at terminal settling conditions. Equation (1) assumes that flocs are fractal aggregates (Kranenburg, 1994), in which

$$\varphi = \left(\frac{D_f}{D_p}\right)^{n_f - 3} ,$$ (2)

φ (dimensionless) is the solid fraction, defined as the volume fraction of the floc composed of mineral sediment grains. The fractal dimension, $n_f \in [1, 3]$ (dimensionless), controls the power law scaling between floc diameter and solid fraction. For

90   the same floc volume, the fractal dimension quantifies the efficiency with which primary particles fill volume due to the structural configuration of primary particles. A compact solid grain is the high efficiency, high fractal dimension end-

member ($n_f = 3$), while a linear chain of primary particles is the low efficiency, low fractal dimension end-member ($n_f = 1$). A typical fractal dimension for natural flocs is ~2 (Kranenburg, 1994; Winterwerp, 1998). Thus, the key inputs in the explicit model are floc diameter, D_f, fractal dimension, n_f, effective primary particle diameter, D_p, and drag ratio, Ω.

95   Effective primary particle diameter, D_p, and drag ratio, Ω, are the outstanding unknowns in the explicit model because prior studies measured floc diameter and fractal dimension (e.g., Jarvis et al., 2005; Strom and Keyvani, 2011), but did not measure D_p and Ω. Cameras are commonly used to measure floc diameter and settling velocity, but the data are limited because regression on the explicit model yields n_f and a coefficient conflating D_p and Ω (Dyer and Manning, 1999; Strom and Keyvani, 2011). More independent data are needed to disentangle the effects of primary particle diameter and drag ratio,

100   the absence of which has led to unverified assumptions about their parametrizations. D_p is typically assumed to be the mean or median of the primary particle size distribution (e.g., Syvitski et al., 1995; Strom and Keyvani, 2011). However, natural flocs contain a primary particle size distribution. Bushell and Amal (1998) proposed a fractal model to account for the distribution:

$$D_p = \left(\frac{\sum D_{pi}^3}{\sum D_{pi}^{n_f}} \right)^{\frac{1}{3-n_f}} , \tag{3}$$

105   where D_{pi} is the diameter of the ith primary particle in the floc. The fractal model predicts the effective primary particle diameter as a function of the primary particle size distribution and fractal dimension. This fractal D_p has the same volume and fills the same n_f-dimensional space as the original primary particles. The fractal model shows that the effective primary particle diameter might be very different from a simple statistical summary of the primary particle size distribution. Equation (3) has been validated using light scattering experiments on synthetic hematite grains (Bushell and Amal, 2000), but has not

110   yet been tested for natural flocs. We tested the fractal D_p theory against estimates of effective primary particle diameter (Sect. 4.5.2 and 4.5.3).

We tested permeability models for the drag ratio, Ω, because they have yet to be directly tested for natural flocs. Strom and Keyvani (2011) used a field and lab data compilation of floc diameter and settling velocity and inferred that more compact flocs ($n_f \geq 2.5$) are impermeable ($\Omega = 1$) but more loosely bound flocs ($n_f < 2$) are appreciably permeable ($\Omega \sim 0.1$ to 0.2).

115   They compared the inferred Ω to drag ratio predictions from the classic Brinkman permeability model (Brinkman, 1947):

$$\xi^{-2} = \frac{1}{6}\left(\frac{D_p}{D_f}\right)^2 \left(1 + \frac{4}{3\varphi} - \sqrt{\frac{8}{\varphi} - 3}\right), \tag{4}$$

Under fractal theory, $\left(D_p/D_f\right)^2 = \varphi^{2/(3-n_f)}$ so the Brinkman model predicts the dimensionless permeability, $\xi^{-2} = 4kD_f^{-2}$, where k (m^2) is the floc permeability, given the solid fraction and fractal dimension. The drag ratio is then $\Omega = [2\xi^2(1 - (\tanh\xi)/\xi)]/[2\xi^2 + 3(1 - (\tanh\xi)/\xi)]$ (Neale et al., 1973). The main obstacle in applying the Brinkman model

120   and many similar permeability models (i.e., Kim and Stolzenbach, 2002) to flocs is that flocs do not fulfill their assumptions of uniform porosity and uniformly sized primary particles. Flocs tend to be less dense at their edges (Eq. 2) owing to their fractal nature and contain a primary particle size distribution. Strom and Keyvani (2011) found that the Brinkman model

overestimates $\Omega \sim 0.75$ to 0.88 for the low-n_f flocs, but it is unclear whether this indicates the Brinkman model is invalid for flocs because they calculated Ω using reported primary particle diameters that might not be valid under fractal theory (Eq. 3).

125   Nonetheless, several floc experiment studies have reported low values of Ω (high permeability) incompatible with standard permeability models (e.g., Johnson et al., 1996; Li and Logan, 1997). Modified permeability models have been proposed to account for the non-uniform pore distribution in fractal aggregates like flocs, in which the largest pores disproportionately enhance permeability (Li and Logan, 2001; Woodfield and Bickert, 2001). In particular, Li and Logan (2001) simply replaced D_p with a larger cluster diameter, D_c (m), in any given permeability equation (e.g., Brinkman model), effectively

130   increasing the solid fraction. The Li and Logan model posits that primary particles are clustered within flocs, so the cluster diameter sets the macropore size and floc permeability. We tested the ability of the original Brinkman model and its Li and Logan modification to predict drag ratio estimates (Sect. 4.5.2).

2.2 Semi-Empirical Model

The semi-empirical model is the Winterwerp (1998) model as modified by Nghiem et al. (2022) to account for the effects of

135   organics, sediment mineralogy, and water chemistry. At equilibrium between floc growth and breakage, the Winterwerp model predicts floc diameter, D_f (m),

$$D_f = \frac{k_A}{k_B} \sqrt{\frac{F_y}{\rho v^2}} C \eta ,\tag{5}$$

in which k_A and k_B (dimensionless) are the empirical floc aggregation and breakage efficiencies, ρ is water density (= 1000 kg m^{-3}), v is water kinematic viscosity (= 10^{-6} m^2 s^{-1}), and C (dimensionless) is the volumetric sediment concentration. The

140   Kolmogorov microscale, η (m), is the length scale of the smallest turbulent eddies in the flow and scales inversely with turbulence intensity (Tennekes and Lumley, 1972). Winterwerp assumed a constant floc yield force $F_y = 10^{-10}$ N (Matsuo and Unno, 1981). Equation (5) is limited because it does not directly include the effects of biota and chemistry on flocculation (Lee et al., 2019; Zeichner et al., 2021).

Nghiem et al. (2022) therefore modified the Winterwerp model to include the effects of organic matter, sediment

145   mineralogy, and water chemistry in k_A/k_B using parametrizations that take advantage of standard geochemical data from river sediment and water samples. The semi-empirical model predicts floc cutoff diameter, D_t (m), which is the threshold grain diameter between significantly flocculated (finer) and unflocculated (coarser) sediment, w_s, and D_f. The model, calibrated on a global river floc data compilation, is

$$D_t = 0.134(\eta D_{p,50})^{1/2}(C_m \theta^2 (1-\theta)^2)^{0.0734}(\text{Al/Si})^{-0.774}\Phi^{-0.180} ,\tag{6a}$$

150    $$w_s = \frac{R_s g D_{p,50}}{20v} 0.306\eta(C_m \theta^2 (1-\theta)^2)^{0.167}(\text{Al/Si})^{-2.15}\Phi^{-0.0358} ,\tag{6b}$$

$$D_f = 0.0180\eta(C_m \theta^2 (1-\theta)^2)^{0.147}(\text{Al/Si})^{-1.55}\Phi^{-0.360} ,\tag{6c}$$

The depth-averaged mud volume concentration, C_m (dimensionless), is assumed to be the representative sediment concentration for flocculation because sand grains are typically not observed in flocs (Lamb et al., 2020; Osborn et al.,

2021). The median primary particle diameter, $D_{p,50}$ (m), is a primary particle grain size metric. Sediment Al/Si (molar ratio)

155   represents sediment mineralogy because clay minerals tend to be enriched in Al/Si compared to feldspar and quartz (e.g., Galy et al., 2008; Bouchez et al., 2014). θ (dimensionless) is the organic cover fraction, the fraction of the sediment grain surface covered with organic matter (Smellie and LaMer, 1958). The relative charge density, Φ (dimensionless), quantifies the effect of salinity and sediment mineralogy on flocculation using diffuse double layer theory (Rommelfanger et al., 2022). Φ is the ratio of cation charges in solution and that at the surface of sediment grains. Flocculation is expected at higher

160   values of Φ where the cation concentration overcomes the negative charges on the surfaces of clay minerals. The semi-empirical model (Eq. 6) provides a complete set of floc predictions in freshwater and complements the explicit model because it relies on hydrodynamic and geochemical data, which are often more readily available than direct floc measurements. However, the semi-empirical model still needs to be verified using observations of floc diameter and settling velocity because they were inferred from sediment concentration-depth profiles to calibrate the model. In this study, we

165   combined geochemical and floc measurements in the Wax Lake Delta to verify the semi-empirical model and constrain the explicit model parameters.

3 Study Site

We conducted fieldwork in the Wax Lake Delta, a river-dominated freshwater delta in the Mississippi River Delta complex (Fig. 1ab). The lower Mississippi River conveys water and sediment to WLD via the Atchafalaya River and Wax Lake

170   Outlet, which was dredged in 1942 (Fig. 1b; Latimer and Schweizer, 1951). The topset of WLD became subaerial after the 1973 Mississippi River flood and has since been aggrading and prograding into the Gulf of Mexico with little human intervention (Roberts et al., 1980; Jensen et al., 2022).
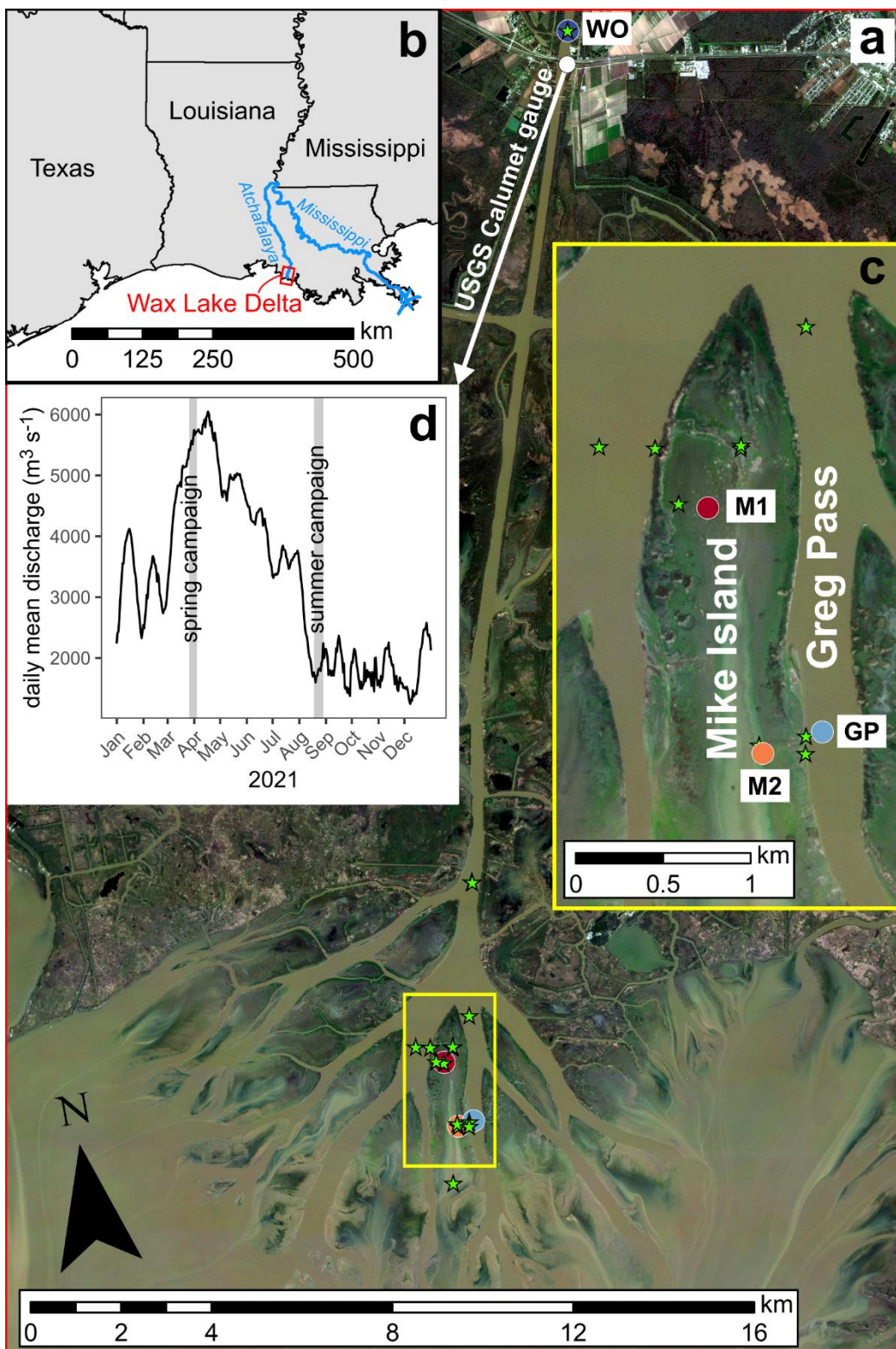
Figure 1: (a) Map of Wax Lake Delta, Louisiana with sample sites. Colored circles indicate main sample sites with sediment concentration-depth and LISST profiles. Green stars indicate additional sediment concentration-depth profile sites without LISST and floc cam measurements. Satellite image is from January 2021, Image © 2021 Planet Labs PBC. (b) Map of Louisiana coast region. (c) Inset map of Mike Island and Greg Pass. (d) 2021 hydrograph of Wax Lake Outlet at Calumet, LA (USGS stream gauge 07381590). Gray bands indicate fieldwork periods.

We completed fieldwork in WLD during March and April 2021 (spring campaign) and August 2021 (summer campaign) as part of the NASA Delta-X project. During the spring campaign, the discharge into WLD was ~5500 m^3 s^{-1}, which is near the peak for 2021 (Fig. 1d). During the summer campaign, the discharge was ~1800 m^3 s^{-1} and close to the low discharge for the year. We studied four sites: Wax Lake Outlet (WO), Greg Pass (GP), northern Mike Island (M1), and southern Mike Island (M2) (Fig. 1ac). Site WO is about 20 km upstream of the delta apex. Site GP is near the center of Greg Pass, the distributary channel east of Mike Island. Sites M1 and M2 on Mike Island are in a tidally-forced shallow wetland. We sampled all sites during the spring campaign, but only sampled site GP during the summer campaign. At each site, we collected vertical profiles of suspended sediment samples (i.e., concentration-depth profiles) and in situ particle size distributions and concentrations with a Sequoia Scientific LISST-200X (LISST) instrument. We collected 8 profiles with paired LISST and sample measurements. We took floc images with a camera system (floc cam) for 4 profiles. We sampled 16 additional concentration-depth profiles distributed throughout WLD without matching LISST or floc cam data, including one profile in October 2019 during a separate field campaign. We also collected water samples to measure major cation and anion concentrations at 20 profile sites and dissolved inorganic carbon (DIC) concentration at 15 profile sites.

4 Methods

We use systematic nomenclature throughout this paper to differentiate between mineral sediment grains, flocs, and a mixture of both. We use the terms "grain" and "sediment" throughout to mean the solid disaggregated mineral sediment, which might or might not have been flocculated in situ. As standard in the flocculation literature, we use "primary particle" to refer to the constituent sediment grains inside flocs. In contrast, we use "particle" alone (i.e., without "primary") to refer generically to the in situ suspended material, which includes flocs and unflocculated sediment.

We used three common floc measurement methods: (1) cameras, (2) in situ particle sizing, and (3) inversion of suspended sediment concentration-depth profiles using the Rouse-Vanoni equation. Flocs are sensitive to their local conditions, so measurements are designed to minimize disturbances. Cameras directly measure floc size and settling velocity (e.g., Mikkelsen et al., 2004; Benson and French, 2007; Osborn et al., 2021), but require reliable image processing algorithms and can be limited by the small number of identifiable flocs. Cameras also cannot detect flocs finer than the pixel resolution, but increasing resolution shrinks the field of view. In situ particle sizing measures in situ particle size distribution and concentration using laser diffraction (e.g., Agrawal and Pottsmith, 2000; Guo and He, 2011), but cannot distinguish between flocs and unflocculated sediment. Although laser diffraction might be sensitive to primary particles within flocs

(Graham et al., 2012), studies have found good agreement between floc size distributions measured by camera and laser diffraction (Mikkelsen and Pejrup, 2001; Mikkelsen et al., 2005). Recent studies have fitted the Rouse-Vanoni equation to
210 grain size-specific suspended sediment concentration-depth profile data to infer depth-averaged floc settling velocity and the grain sizes within flocs (Lamb et al., 2020; Nghiem et al., 2022). However, this technique relies on the sediment diffusivity ratio parametrization, is indirect, and cannot measure floc diameter.

We used all three methods to measure floc diameter and settling velocity (Sect. 4.1-4.3). First, we identified the floc cutoff diameter by inverting grain size-specific concentration-depth profiles with the Rouse-Vanoni equation (Sect. 4.4).
215 With these floc constraints, we combined the data sources to estimate explicit model variables (Table 1; Sect. 4.5): floc solid fraction, fractal dimension, drag ratio, and effective primary particle diameter. We collected a suite of water and sediment geochemistry data as inputs into the semi-empirical model (Sect. 4.6).

Table 1: Estimated floc variables and their data sources. The variables are listed by order in the data processing workflow. In the
220 **Data Source column, "sediment" refers to grain size distribution, concentration, and Rouse-Vanoni fitting data from individual suspended sediment samples and sediment concentration-depth profiles. The primary data source (if any) is listed first. In the Description column, the data sources are indicated in parentheses next to input variables for variables with multiple data sources.**

Variable	Data Source	Description	Section or (Equation)
Paired diameter (m) and settling velocity (m s^{-1}) of individual flocs	floc cam	Diameter: Extracted using image analysis Settling velocity: Calculated by manually tracking particles	4.3
Floc cutoff diameter, D_t (m)	sediment	Selected by eye from grain diameter-settling velocity results from Rouse-Vanoni fitting of grain size-specific concentration-depth profiles	4.5.1
Floc size distribution (m) and concentration	LISST, sediment	Particle size distribution and concentration (LISST) removing the unflocculated sediment fraction in the classes coarser than D_t (sediment)	4.5.1
Primary particle size distribution (m) and concentration	sediment	Grain size distribution and sediment concentration removing the fraction coarser than D_t	4.5.1
Bulk solid fraction, $\bar{\varphi}$	sediment, LISST	Ratio of primary particle (sediment) and floc concentrations (LISST, sediment)	4.5.1
Fractal dimension, n_f	LISST, sediment	Calculated such that the bulk solid fraction	4.5.2

		across the floc size distribution (LISST, sediment) equals the calculated $\bar{\varphi}$ (sediment, LISST)	(10)
Effective primary particle diameter, D_p (m)	LISST, sediment	Calculated using n_f (LISST, sediment) and $\bar{\varphi}$ (sediment, LISST)	4.5.2 (8b)
Drag ratio, Ω	floc cam, LISST, sediment	Calculated using floc cam-measured floc diameter and settling velocity (floc cam) by solving the floc settling velocity equation (Eq. 1) for Ω with the calculated n_f (LISST, sediment) and D_p (LISST, sediment)	4.5.2 (1)
Floc settling velocity distribution (m s^{-1})	LISST, floc cam, sediment	Converted floc size distribution (LISST, sediment) using the floc settling velocity equation (Eq. 1) with calculated Ω (floc cam, LISST, sediment), n_f, and D_p (both LISST, sediment)	4.5.2 (1)

4.1 Suspended Sediment Sampling and Hydrodynamic Measurements

We briefly summarize our suspended sediment sampling methods, which are documented in full in Nghiem et al. (2021). For each profile, we collected suspended sediment samples at different heights above the bed from a boat with an 8.2-L Van Dorn sampler. Each profile took about 40-60 min to sample in full. At the channel sites (WO and GP), we collected samples while drifting over the target location to sample isokinetically (Edwards and Glysson, 1999) and minimize sampling bias. In contrast, we sampled while stationary at the wetland sites (M1 and M2) because the airboat used for sampling could not drift with the current. We expect that these samples are still representative of the in situ suspended sediment because of the relatively slow depth-averaged flow velocities inside the wetland (~0.1 m s^{-1}). We also collected concurrent flow velocity profile measurements with a Teledyne RiverPro acoustic Doppler current profiler (ADCP) instrument. We filtered each sample through 0.2 μm pore size polyethersulfone filter paper (Sterlitech). We froze the filtered sediment until ready for lab analysis. In the lab, we measured the sediment concentration and grain size distribution of each suspended sediment sample. We oven-dried and weighed each sample to calculate the sediment concentration as the ratio of the sediment mass and total sample volume. We discarded data in which the calculated sediment concentration is anomalously low or high compared to other samples in the same profile because these samples are not representative of the in situ steady state sediment concentration. We decarbonated, oxidized, and deflocculated an aliquot of each sediment sample for grain size analysis (Douglas et al., 2022). We measured the volume-based grain size distribution (i.e., fully dispersed sediment grains) using a

Malvern Mastersizer 3000E laser diffraction particle size analyzer with the non-spherical scattering model from 0.2 to 2100
240   μm in 100 logarithmically spaced bins.

We estimated the boundary shear velocity, u_* (m s^{-1}), for each profile by fitting the measured ADCP flow velocity profile to the law of the wall (e.g., García, 2008). The law of the wall is commonly used to model the flow velocity profile through the entire depth, but is only strictly valid in the bottom 20% of the flow depth (Nezu and Nakagawa, 1993). ADCP data quality declines near the bed, so we fitted the law of the wall using both the full flow velocity and the truncated flow
245   velocity profile in the bottom 20% depth. We chose the fit that had the higher coefficient of determination and calculated the shear velocity from the fitted coefficients. We calculated the Kolmogorov microscale, η (m), using the shear velocity. The Kolmogorov microscale is $\eta = (\nu^3/\varepsilon)^{1/4}$, where ε (m^2 s^{-3}) is the dissipation rate of turbulence kinetic energy per unit mass. We used $\varepsilon = (u_*^3/\kappa)(1/z - 1/h)$ where κ (dimensionless) is the von Kármán constant (= 0.41), z (m) is height above the bed, and h (m) is the water depth (Nezu and Nakagawa, 1993).

250   **4.2 In Situ Particle Size Distribution and Concentration Measurements**

We briefly summarize our methods for measuring in situ particle size distribution and concentration, which are documented in Fichot and Harringmeyer (2021). We used a LISST-200X instrument to measure in situ particle size distribution and concentration. The LISST measures the particle volume concentration in 36 logarithmically spaced size bins (1 to 500 μm) using laser diffraction at a rate of 1 Hz (Sequoia Scientific, 2022). We deployed the LISST attached to a rope from a
255   boat in drift and measured downcast profiles to the bottom or the end of the rope by lowering the LISST at a rate of about 0.1 m s^{-1}. Angular scattering intensity of the laser was inverted to calculate suspended particle size distribution using the manufacturer-provided software set for non-spherical particles.

4.3 Floc Imaging

We measured diameters and settling velocities of flocs with a custom-built imaging device called the "floc cam" (Fig. 2a).
260   The floc cam is a frame on which we mounted a camera and a modified 2.2 L Van Dorn sampler. We installed a 7 cm diameter window on the side of the sampler through which a backlight illuminates the interior. On the opposite side, we installed a 3 cm diameter window through which a camera can take photos. We painted the interior of the sampler black to minimize light reflection. We installed two 10 cm tall half-pipes of 1 in PVC pipe in the sampler to increase interior surface roughness and reduce turbulence of collected samples. For each floc cam sample, we followed the same procedure for
265   suspended sediment sampling up until the sample was retrieved from depth. Then, we mounted the sampler in the floc cam frame and took photos of backlit particles within the sampler using a mounted camera (Nikon D750) equipped with an AF-S Micro NIKKOR 60 mm f/2.8G ED lens (Fig. 2a). We programmed the camera to take photos at a rate of 4 Hz (0.25 s interval). Once the sampler and camera were in place, we covered the entire frame with a black tarp to shield the camera from ambient light. The time between sample collection and the start of image collection was typically ~1 min. We allowed

270   the camera to take photos for a few minutes, yielding an image time series for each floc cam sample. We calibrated one pixel
per 6 μm in the focal plane of the camera.
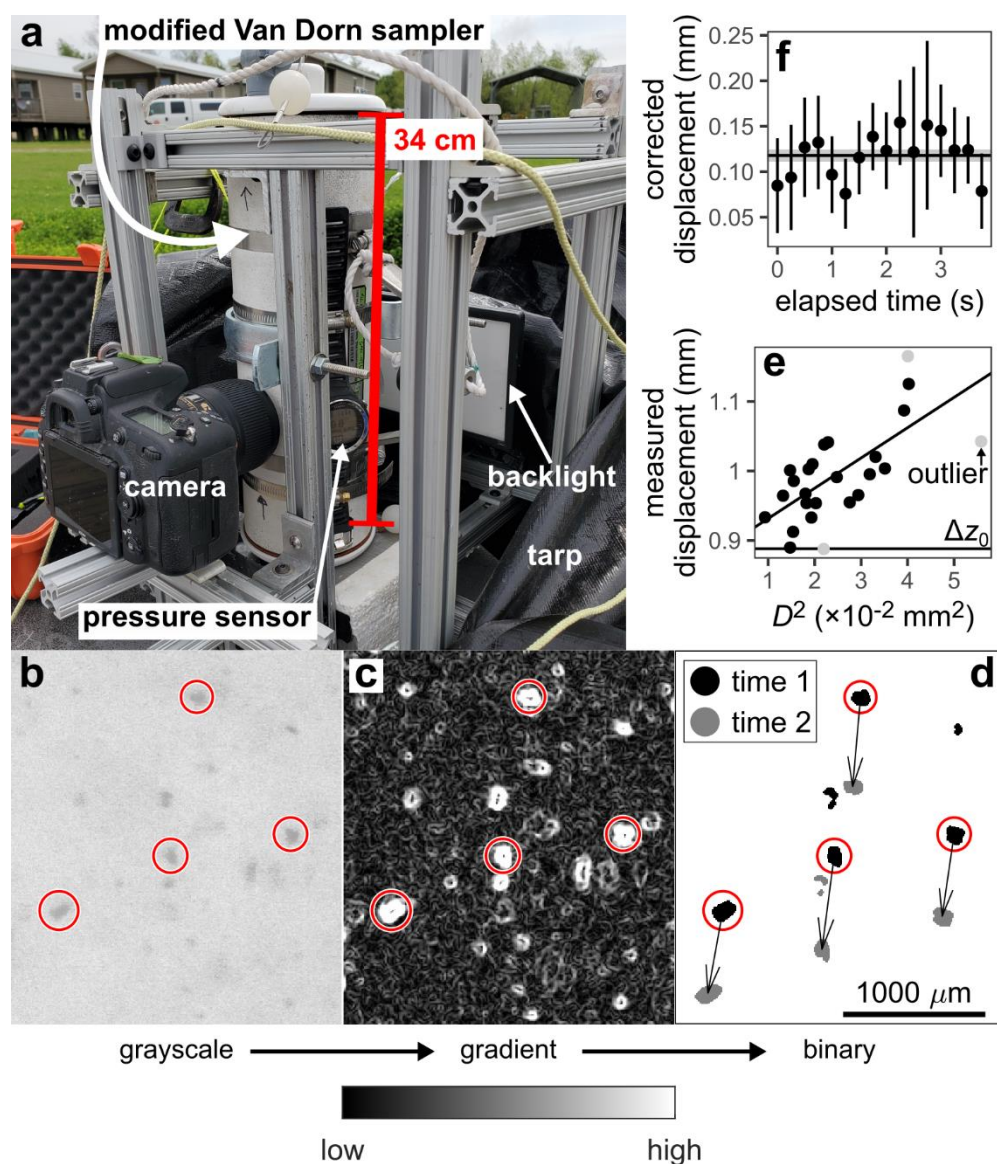
Figure 2: Floc cam data collection and processing. (a) Floc cam setup. During image collection, the black tarp covered the sampler
275   **and frame to block external light. (b) Example floc cam grayscale image of particles. (c) 2D gradient of the grayscale image. High-**
gradient pixels correspond to particle borders. (d) Binarized particles showing particle displacement between an image pair. Scale
in panel d also applies to panels b and c. (e) Example scatterplot of squared diameter, D^2, and measured displacement. Δz_0
indicates the fitted background correction. (f) Time series of corrected displacement for a single tracked particle across multiple
image pairs. The corrected displacement isolates the displacement due to gravitational settling.

280

We detected particles in each image time series with the MATLAB Image Processing Toolbox following a gradient-based method to detect and remove out-of-focus particles (Keyvani and Strom, 2013). We converted each image in a time series to grayscale and cropped the image to a smaller area of interest. We rescaled the pixel values in the cropped image and applied a Gaussian smoothing filter (Fig. 2b). Next, we took the gradient of the image with a central difference method (Fig. 2c). We

285 binarized the gradient image using an empirically-determined gradient cutoff to exclude any particles where the gradient was too small (i.e., the particle was out-of-focus; Fig. 2d). We applied morphological erosion and dilation on the binary image to remove noise speckles and connect fragments belonging to the same particle. Finally, we filled holes within the particles because the gradient method identifies particle edges.

We tracked particles manually between successive frames using the processed binary images of in-focus particles

290 (Fig. 2d) to calculate settling velocity. We identified the same particle across frames according to particle size, shape, and displacement. We tracked 100 unique particles for each image time series over an image time span of 10 to 20 s and only recorded particles that could be tracked for at least three consecutive frames. The mean number of frames over which we tracked particles is 7.4. For each tracked particle, we calculated the diameter as the diameter of an equal-area circle using the second-largest measured particle area to limit the effect of outliers. Background currents affected particle motion because

295 settling velocities calculated with measured displacements were unrealistically high and, in some cases, particles moved upward. We used a regression method to isolate particle displacement due to gravitational settling in which we assumed that background currents perfectly advected particles (Smith and Friedrichs, 2015). Under this assumption, the particle displacement between an image pair is $\Delta\hat{z} = \Delta z + \Delta z_0$ where $\Delta\hat{z}$ (m) is the observed vertical displacement of the particle, Δz (m) is the displacement due to gravitational settling, and Δz_0 is the displacement due to background currents. Stokes law

300 predicts that the gravitational displacement in a given time scales with the square of particle diameter, D. We assumed that Δz_0 is independent of particle size because the particles are sufficiently small. Combining the data of all tracked particles in an image pair, we regressed $\Delta\hat{z}$ against D^2 according to the equation $\Delta\hat{z} = cD^2 + \Delta z_0$ (Fig. 2e). We recovered Δz_0 as the intercept and solved for Δz (Fig. 2f) for all particles and consecutive image pairs. We discarded the data for which $\Delta\hat{z}$ fell into the 95% confidence interval of the estimated Δz_0 because the uncertainty relative to $\Delta\hat{z}$ precludes resolution of Δz for

305 these data. 222 out of an initial 400 total tracked particles remained (~56%) after this filtering. Floc porosity and permeability might be responsible for the uncertainty because they also affect settling velocity. For each particle, we calculated settling velocity as the mean of Δz divided by the time interval between images.

4.4 Rouse-Vanoni equation inversion of concentration-depth profiles

Rouse-Vanoni equation fits to grain size-specific concentration-depth profiles provide floc cutoff diameter and depth-

310 averaged floc settling velocity estimates (Lamb et al., 2020; Nghiem et al., 2022). The Rouse-Vanoni equation models the suspended sediment concentration as a function of height from the bed, z, in a flow of depth h assuming a balance of gravitational sediment settling and upward turbulent sediment fluxes (Rouse, 1937):

$$\frac{C_i}{C_{bi}} = \left(\frac{\frac{h-z}{z}}{\frac{h-h_b}{h_b}} \right)^{p_i},$$ (7)

where C_i (dimensionless) is the sediment volume concentration, C_{bi} (dimensionless) is the sediment volume concentration at

315   the near-bed height h_b (m), p_i (dimensionless) is the Rouse number, and the subscript i denotes the ith grain size class. Vertical concentration stratification increases with Rouse number, $p_i = w_{si}/(\kappa\beta u_*)$, where w_{si} (m s⁻¹) is the in situ grain size-specific settling velocity. The diffusivity ratio, β (dimensionless), is the ratio of turbulent sediment diffusivity and turbulent momentum diffusivity and accounts for the fact that sediment does not exactly follow turbulent eddies (e.g., García, 2008). If β and u_* are known, then w_{si} can be calculated from the fitted p_i. Past studies using this method have

320   interpreted the inferred settling velocity for fine silt and clay grain sizes as a depth-averaged floc settling velocity because it is much faster than the settling velocity theory prediction for individual grains (Lamb et al., 2020; Nghiem et al., 2022). Nghiem et al. (2022) used these inferred floc settling velocities to calibrate the semi-empirical model and identify the floc cutoff diameter, D_t. Sediment finer than D_t is significantly flocculated, while sediment coarser than D_t is not significantly flocculated.

325   β is an obstacle to calculating w_{si} because its exact form is unknown (De Leeuw et al., 2020; Lamb et al., 2020). Prior studies invoked sediment-induced density stratification (Wright and Parker, 2004; Moodie et al., 2020) and grain size-dependent momentum effects to model β (Carstens, 1952; Csanady, 1963; Graf and Cellino, 2002). However, it is unknown whether these formulations for solid grains apply to the diffusivity ratio for flocs, β_{fl}. In past work, β_{fl} was extrapolated from relations for the sand diffusivity ratio for sand (De Leeuw et al., 2020; Lamb et al., 2020; Nghiem et al., 2022). Recent work

330   showed that β_{fl} is typically smaller than 1 and increases with w_{si}/u_* (Izquierdo-Ayala et al., 2021, 2023; Egan et al., 2022), but is limited because the floc concentration was calibrated from acoustic backscatter data without partitioning by floc size and settling velocity.

Following Lamb et al. (2020) and Nghiem et al. (2022), we fitted the log-linearized Rouse-Vanoni equation to grain size-specific concentration-depth profiles (e.g., profiles of the dispersed, unflocculated sediment) from the concentrations

335   and grain size distributions of the suspended sediment samples. We converted the sediment mass concentrations to volume concentrations assuming a sediment density of 2650 kg m⁻³ and used $h_b = 0.1h$ (De Leeuw et al., 2020). For each grain size class, we computed the grain size-specific concentration as the total sediment concentration times the volume fraction in the size class from the grain size distribution (Sect. 4.1). We estimated the grain size-specific Rouse number, p_i, from the Rouse-Vanoni equation fits for each grain size class and each sediment concentration-depth profile. We used shear velocity

340   estimates from ADCP flow velocity profiles (Sect. 4.1), assumed $\beta = 1$ as a starting point to approximate w_{si}, and identified D_t. We calculated the Rouse-estimated floc settling velocity as the median w_{si} within grain diameters finer than D_t.

4.5 Estimating floc properties

4.5.1 Floc size distribution, concentration, and bulk solid fraction

For each profile, we matched each suspended sediment sample (representing the dispersed sediment grains) to a set of LISST
345   measurements to obtain the coinciding in situ particle concentration and size distribution (representing the in situ suspended particles). For each suspended sediment sample, we assigned all the LISST measurements collected within 0.1 m (the sampler radius) of the collection depth. If there were no LISST measurements in this range, then we assigned the 3 LISST measurements closest in depth. We combined the assigned LISST measurements by taking the mean of the concentration in each particle size class. For each profile, we also composited the distributions over all samples to calculate depth-averaged
350   distributions.

We removed the contribution of unflocculated sediment from the LISST particle size distributions, which measured both flocs and unflocculated sediment, to calculate floc size distributions (Table 1). We used the fact that sediment grains coarser than D_t are significantly unflocculated (Lamb et al., 2020; Nghiem et al., 2022). We identified D_t from the grain size-specific Rouse-Vanoni equation fitting results by eye (Sect. 4.4; Nghiem et al., 2022). For each LISST particle size class
355   above the floc cutoff diameter, we calculated the volume concentration of unflocculated material in that class using the corresponding grain size distribution and sediment concentration (Sect. 4.1; Table 1). We subtracted the unflocculated concentrations from the LISST particle concentrations to isolate the floc volume concentration and normalized them to obtain floc size distributions.

We obtained the primary particle volume concentration and size distribution using the portion of the grain size
360   distribution and sediment volume concentration finer than the floc cutoff diameter (Table 1). We calculated the median primary particle diameter, $D_{p,50}$ (m), as the median of the distribution. We calculated the floc bulk solid fraction, $\bar{\varphi}$ (dimensionless), as the ratio of the primary particle and floc volume concentrations (e.g., Mikkelsen and Pejrup, 2001; Guo and He, 2011).

4.5.2 Fractal dimension, effective primary particle diameter, and drag ratio

365   For each suspended sediment sample in the concentration-depth profiles, we identified the fractal dimension, n_f, and effective primary particle diameter, D_p, for the integrated floc settling velocity across the floc size distribution to match the mean settling velocity (Table 1). The mean settling velocity and bulk solid fraction are

$$\overline{w_s} = \sum_{i=1}^n f_i w_{si} \, , \tag{8a}$$

$$\bar{\varphi} = \sum_{i=1}^n f_i \left(\frac{D_{fi}}{D_p}\right)^{n_f - 3} , \tag{8b}$$

370   where f_i is the volume fraction in the ith floc size class, n is the number of floc size classes (= 36), and $\overline{w_s}$ (m s⁻¹) is the mean floc settling velocity. For simplicity, we neglected inertial effects in the explicit model because we calculated a typical floc

Reynolds number of ~0.5, for which inertial effects are small (~5% increase in drag coefficient compared to the purely viscous model). As such, $\overline{w_s}$ follows the explicit model except with mean values:

$$\overline{w_s} = \frac{R_s g \overline{\varphi} \overline{D_f}^2}{b_1 \Omega \nu},$$ (9)

375 where $\overline{D_f}$ (m) is the mean floc diameter calculated logarithmically from the floc size distribution. We combined Eq. (8) and (9) to eliminate the unknown D_p and obtained

$$\frac{\sum f_i D_{fi}^{n_f-1}}{\sum f_i D_{fi}^{n_f-3}} = \overline{D_f}^2,$$ (10)

This approach assumes that a single D_p describes the primary particle diameter across the whole floc size distribution. In reality, the primary particle diameter probably varies with floc diameter (Nicholas and Walling, 1996), but

380 the relationship is poorly known. For each sample, we solved Eq. (10) for fractal dimension with a root-finding algorithm and calculated the effective primary particle diameter using Eq. (8b) with the fitted n_f (Table 1). We estimated uncertainty on floc concentration, n_f, and D_p as the 95% bounds on the bootstrap distribution from 1000 resampling replicates with replacement of the matched set of LISST measurements (Sect. 4.5.1). We divided the floc settling velocity model prediction (Eq. 1 explicit model using the calculated D_p and n_f and setting $\Omega = 1$ and $b_1 = 20$) by the measured settling velocity for

385 each floc cam observation to calculate Ω.

4.5.3 Testing effective primary particle diameter theory

We compared the calculated effective primary particle diameter and fractal primary particle diameter to test the fractal D_p model (Eq. 3). We evaluated the fractal D_p model using simulations of primary particle diameters contained within flocs. We used the number distribution, rather than volume distribution, of primary particle size because discrete particles are the

390 fundamental units in floc growth. For each suspended sediment sample, we constructed the number distribution by dividing the volume fraction in each size class by the cube of the grain diameter and renormalizing to ensure the fractions sum to 1. For each sample, we simulated 10,000 flocs each containing a number of primary particles determined by fractal theory, $n_p = (D_f/D_p)^{n_f}$ (Kranenburg, 1994) where n_p is the number of primary particles in a floc. For each iteration, we first sampled a floc diameter from the number-based floc size distribution. Using the fitted n_f and D_p, we calculated and sampled

395 n_p primary particle diameters from the number-based primary particle size distribution. We summarized the sampled primary particle diameters using Eq. (3) and the median and then further summarized each set of primary particle diameters with a volume-weighted mean. Equation (3) is limited because the number of primary particles in a floc must be known. As such, we tested a simplified fractal model in which we assumed the number of primary particles is sufficiently large for the central limit theorem to apply, yielding

400 $$D_p = \left(\overline{D_p^3}/\overline{D_p^{n_f}}\right)^{1/(3-n_f)},$$ (11)

where the overbars denote taking the mean of the distribution (Gmachowski, 2003).

4.6 Geochemical Measurements

We measured the Al/Si and total organic carbon (TOC) of sediment and major ion concentrations and dissolved inorganic carbon (DIC) concentration of river water to calculate Al/Si, θ, and Φ in the semi-empirical model following Nghiem et al.
405 (2022). We measured sediment Al/Si using X-ray fluorescence (XRF) for 33 samples (Appendix A). We calibrated a model between grain size and Al/Si ($R^2 = 0.88$) and used it to calculate Al/Si for each concentration profile using the depth-averaged grain size distribution (Fig. A1). We measured TOC in the suspended sediment samples to calculate θ. The sediment samples were leached with 2 M HCl at 80°C to remove carbonate and then oven-dried. TOC content was measured on the decarbonated samples using an Exeter Analytical CHN analyzer with uncertainties determined from repeat
410 measurements of reference materials. Samples were weighed before and after decarbonation to determine the fraction of sediment mass lost during decarbonation. This fraction was used to convert the raw measured TOC concentrations to the corrected values for pre-decarbonated samples. We assumed the organic matter is cellulose to convert TOC concentration to organic matter concentration (Nghiem et al., 2022).

We used ion chromatography and cavity ring-down spectroscopy to measure the major ion concentrations (cations:
415 Na^+, K^+, Ca^{2+}, Mg^{2+}; anions: Cl^-, HCO_3^-, SO_4^{2-}) of water samples as inputs to calculate Φ. Major cation (Na^+, K^+, Ca^{2+}, Mg^{2+}) and anion (Cl^-, SO_4^{2-}) concentrations were measured by ion chromatography at Durham University (Geography Department) and checked by regular measurements of the LETHBRIDGE-03 standard. The dissolved inorganic carbon (DIC) concentration was determined using a Picarro Cavity-Ring Down Spectroscopy (CRDS) G2131-i coupled to a modified AutoMate autosampler. About 6 mL of filtered river water was injected through a 0.2 μm syringe filter into an
420 evacuated and pre-weighed 12 mL AutoMate exetainer. The AutoMate acidified the samples with 10% phosphoric acid. The resulting CO_2 was carried in a nitrogen stream into the Picarro CRDS for total carbon measurements (Dong et al., 2018). DIC concentration was calibrated against weighed optical calcite standard reference materials that were acidified in evacuated exetainers with 10% phosphoric acid overnight. We assumed that all DIC was HCO_3^- to convert the measured DIC concentrations to HCO_3^- concentrations. We solved for the HCO_3^- concentration using charge balance for cases in
425 which we had ion chromatography measurements, but did not measure DIC concentration.

5 Results

First, we describe the basic hydrodynamics, sediment properties, and floc observations from the individual measurement methods (Sect. 5.1-5.4). Then, we analyze the effective primary particle diameter and drag ratio in the explicit model. To this end, we combine results from the multiple floc methods to derive floc variables (Sect. 5.5 and 5.6), which we use to estimate
430 the effective primary particle diameter and drag ratio, compared them to theory, and validate using floc settling velocity inferred from the Rouse-Vanoni equation fitting (Sect. 5.6-5.8). Finally, we validate the semi-empirical model and use it as a framework to examine the environmental factors responsible for the observed floc properties in WLD (Sect. 5.9).

5.1 Hydrodynamics

The sampled profiles span a wide hydrodynamic range in WLD because of discharge seasonality and environment (Fig. 1d;
435 Table 2). The fastest flow occurred at site WO in the spring (~1.5 m s⁻¹ depth-averaged) far upstream of the delta apex in the
Wax Lake Outlet, where the water depth was also the greatest (30 m) among the sampled sites. Further down the delta, the
distributary channel site GP had slower flow velocity (~0.58 m s⁻¹ depth-averaged in the spring) and depth (~3 to 4 m). At
site GP, the depth-averaged flow velocity in the summer was about half (~0.2 to 0.3 m s⁻¹) of that in the spring because of the
discharge seasonality (Fig. 1d). The island sites were sampled in the spring only. These sites had the slowest flow velocities
440 (0.024 and 0.11 m s⁻¹) out of the sampled sites because the flow was unchannelized (water depth ~0.6 m). The shear velocity
generally increased with the flow velocity, ranging from ~0.3 (in the island) to ~9 cm s⁻¹ (in Wax Lake Outlet during spring
high-flow conditions). The Kolmogorov microscale varied inversely with the shear velocity from 260 to 1300 μm.

**Table 2: Metadata and hydrodynamic data of sampled profiles. Boldface profile name indicates that we collected floc cam images
445 for the profile. Shear velocity uncertainty indicates the 95% confidence interval on the law of the wall fit (Sect. 4.1).**

Profile name (Site + season + index)	Date (yyyy-mm-dd)	Number of suspended sediment samples	Water depth (m)	Depth-averaged flow velocity (cm s⁻¹)	Shear velocity (cm s⁻¹)	Depth-averaged Kolmogorov microscale (μm)	Depth-averaged suspended sediment volume concentration (×10⁻⁵)
GP spring 1	2021-03-27	8	3.8	58	5.6 ± 0.03	260	5.2
WO spring	2021-03-30	4	30	150	9.2 ± 0.006	290	7.3
M2 spring	2021-04-02	4	0.64	11	1.7 ± 0.07	400	5.3
M1 spring	2021-04-02	4	0.59	2.4	0.34 ± 0.08	1300	4.7
GP spring 2	2021-04-02	4	3.5	58	4.8 ± 0.03	280	5.7
GP summer 1	2021-08-18	4	3.4	26	3.2 ± 0.04	380	0.73
GP	2021-08-	5	3.4	32	1.6 ± 0.06	640	0.61

summer 2	20						
GP summer 3	2021-08-22	10	3.2	23	2.4 ± 0.02	470	0.61

5.2 Concentration-depth profiles

The concentration-depth profile results inform the concentrations, grain size distributions, and flocculation state of the suspended sediment. In general, the depth-averaged suspended sediment is muddy (~90% mud by volume) and more concentrated in the spring (~5 to 7×10^{-5} volume concentration) than in the summer (~5 to 6×10^{-6}) because of the discharge

450   seasonality (Table 2).

The grain size-specific sediment concentration-depth profiles reveal a stratification trend of higher concentration closer to the bed for both mud and sand grain size classes, a pattern consistent with the Rouse-Vanoni equation (Eq. 7). Figure 3a shows an example of the grain size-specific profiles for the profile GP spring 1. Sand tended to be more stratified than mud, with the coarsest sand (~100 to 200 µm) so severely stratified that it was effectively absent in samples higher in

455   the water column. Mud was appreciably stratified compared to the expectation of a nearly uniform concentration profile from the Rouse-Vanoni equation for the slowly settling unflocculated mud. The vertical variability is likely due to natural variability in sediment concentration and the fact that we collected samples over a period of 40 to 60 min (Fig. 3a).
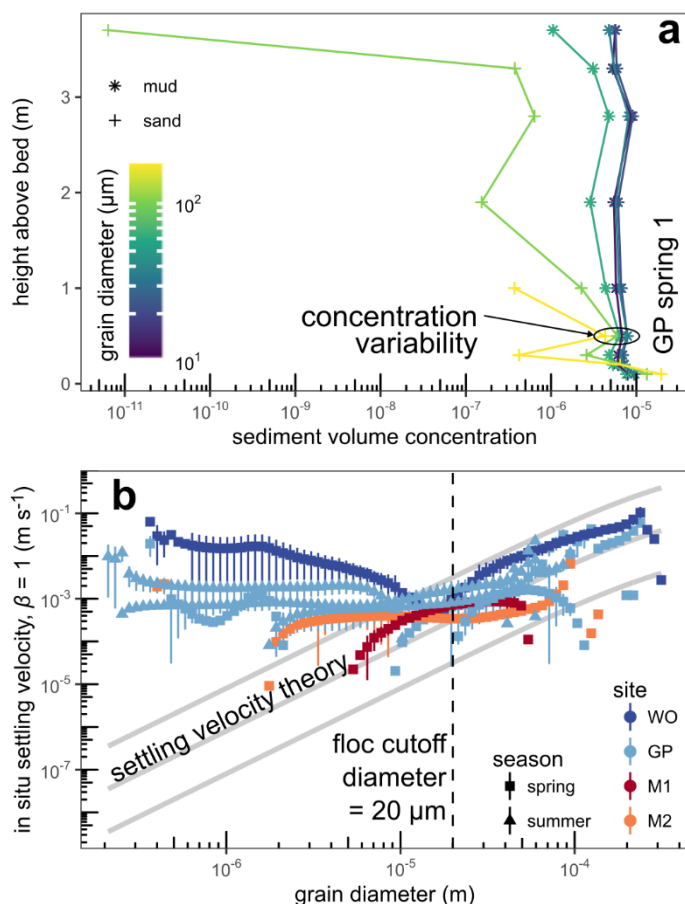
Figure 3: Rouse-Vanoni equation inversion results for profiles with paired suspended sediment samples and LISST measurements. (a) Example of sediment volume concentration as a function of height above bed for profile GP spring 1. We used the full 100 grain size classes in all calculations, but reclassified the data into 6 classes for this panel only to improve readability. The relatively high concentration at 0.5 m above the bed is an example of natural sediment concentration variability. (b) Grain diameter and Rouse-estimated in situ settling velocity using $\beta = 1$. The gray settling velocity theory curves indicates the Ferguson and Church (2004) model with an order-of-magnitude above and below. Vertical bars represent the propagated 68% confidence interval on the Rouse number estimates. Points without vertical bars have confidence intervals that overlap with 0.

The grain diameter versus in situ settling velocity trend from the Rouse-Vanoni equation fitting shows that sediment finer than ~20 μm was appreciably flocculated at the main sample profiles (Fig. 3b), assuming that the sediment and floc diffusivity ratios are unity. This floc cutoff diameter indicates the grain diameter at which the in situ mud settling velocity departs from settling velocity theory prediction ($w_s = (R_s g D^2)/(c_1 \nu + \sqrt{0.75 c_2 R_s g D^3})$ for grain diameter, D, $c_1 = 20$, and $c_2 = 1.1$; Ferguson and Church, 2004). The faster in situ velocity (than the prediction) in the sediment finer than the floc cutoff diameter is consistent with the results of Lamb et al. (2020) and Nghiem et al. (2022) indicating that flocculation is

responsible. Conversely, the in situ settling velocity follows settling velocity theory well for grain diameter larger than about
475 20 μm and indicates that this coarser sediment is not substantially flocculated. Although the $\beta = 1$ assumption makes the
precise in situ settling velocity values inaccurate, we expect the floc cutoff diameter to be robust because it marks an abrupt
change in the settling velocity pattern. We used 20 μm as the floc cutoff diameter to calculate floc size distributions for this
set of profiles with corresponding LISST measurements (Sect. 4.5.1).

5.3 LISST Particle Size Distribution and Concentration

480 The combined size distributions and concentrations of flocs and unflocculated sediment (i.e., in situ particles) from LISST
profiles indicate limited vertical variation of median particle diameter and concentration, but the much larger median particle
diameter compared to median grain diameter (3 to 30 times) supports the occurrence of flocculation (Fig. 4). The channel
sites (WO and GP) had median particle diameters of ~50 to 90 μm, while the island sites (M1 and M2) had median particle
diameters of ~35 μm (Fig. 4a). Although the vertical variation in total particle concentration was broadly limited, the
485 concentration increased slightly toward the bed in some profiles (Fig. 4b). In the spring, the particle volume concentration
was about 3 to 5×10^{-4} for all sites except for the site M1, which had a slightly smaller concentration of ~2 to 3×10^{-4}. In the
summer, the particle volume concentration at site GP was much smaller, ~5 to 8×10^{-5}, because of the smaller summer
discharge. However, the depth-averaged particle size distributions were similar across the channel sites for both the spring
and summer (Fig. 4c). The island distributions were skewed toward finer particles. The fraction of particles coarser than the
490 floc cutoff diameter ranges from ~0.6 to 0.85, indicating that the concentration in most LISST size classes might need to be
corrected for unflocculated sediment to retrieve the floc concentration and size distribution. The median depth-averaged
particle diameter ranges from about 3 to 30 times larger than the median grain diameter (Fig. 4d), an effect that we attribute
to flocculation.
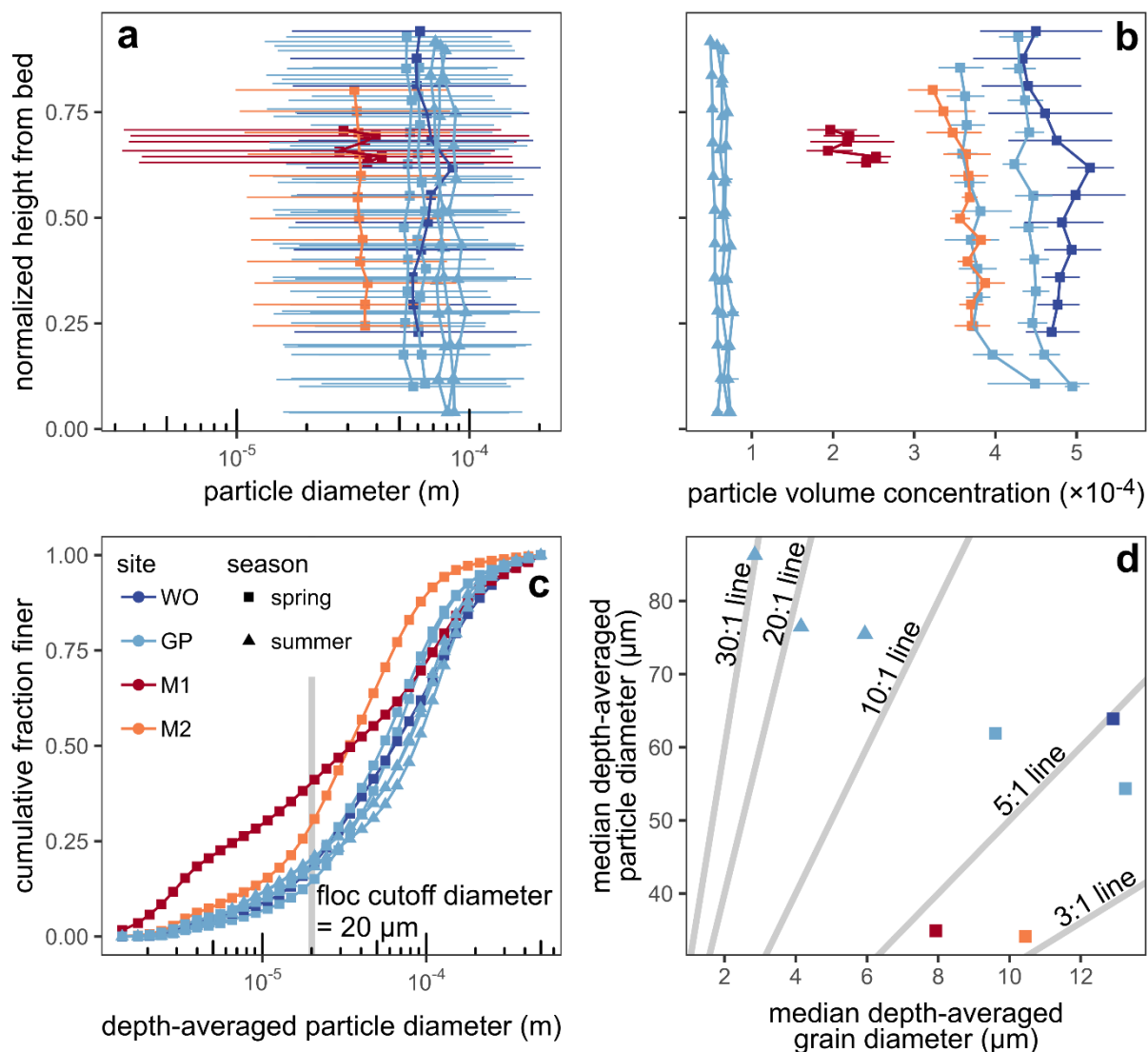
Figure 4: LISST results. (a) Profiles of in situ particle diameter. Points represent the median particle diameter. Horizontal bars represent the span of the D_{16} and D_{84} particle diameters, the diameters for which 16% and 84% of particles are finer, respectively. (b) Profiles of in situ particle volume concentration. Horizontal bars represent the 95% bootstrap uncertainty. (c) Cumulative distribution functions of depth-averaged particle diameter. (d) Scatterplot of median grain diameter and median particle diameter. The legend in panel c applies for all panels.

5.4 Floc Cam

We extracted direct measurements of particle diameter and settling velocity from the floc cam images, with diameters of ~70 to 200 μm and settling velocities of ~0.1 to 1 mm s^{-1}. We could not verify visually from the images whether the tracked

particles were flocs, so we compared the relationship between diameter and settling velocity measurements to settling
505   velocity theory for solid grains (Ferguson and Church, 2004). For a given diameter, the measured settling velocities are
slower than the settling velocity predictions of solid grains as expected because flocs are porous and hence less dense than
sediment (Fig. 5). Conversely, the measured floc settling velocities are about one order-of-magnitude faster than the
predicted settling velocity of a typical 5-µm mud primary particle. These comparisons confirm that the tracked particles were
indeed flocs. The floc cam data show the expected trend of increasing floc settling velocity with floc diameter (Eq. 1), but
510   there is considerable scatter probably because of density variations and inherent stochasticity of flocculation (see discussion
in Strom and Keyvani, 2011).
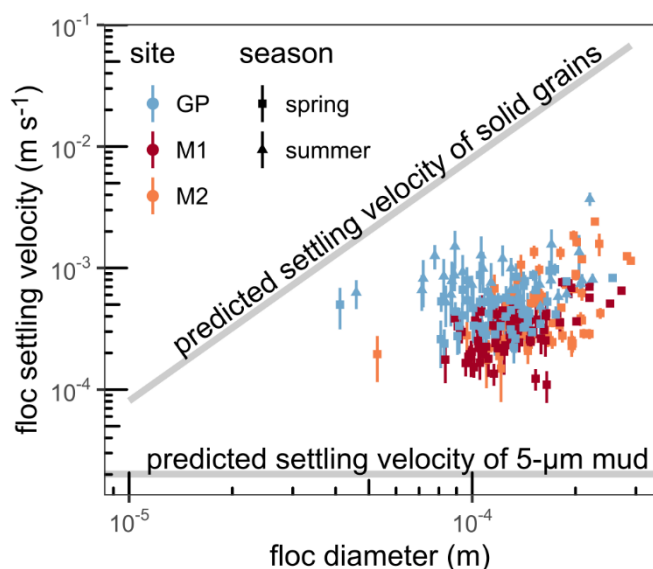
Figure 5: Floc cam-measured floc diameter and floc settling velocity. Vertical bars indicate the propagated mean standard error
515   **on the background displacement estimate (Sect. 4.3).**

5.5 Floc Size Distribution and Concentration

We combined the individual data sources (Sect. 5.1-5.4) to compute floc variables, starting here with the floc concentration
and size distribution. We assumed that the LISST particle concentration and size distribution (Sect. 5.3) include
unflocculated sediment in the particles coarser than the floc cutoff diameter of 20 µm (Sect. 5.2). Thus, we removed the
520   sediment concentration coarser than 20 µm from the LISST particle size distributions and concentrations to isolate the floc
size distributions and concentrations (Table 1).

        The floc data show limited vertical variation of median diameter and concentration (similar to the raw LISST
results) and indicate that flocs were ~1 to 100 µm in diameter and predominately smaller than the Kolmogorov microscale.
The total floc concentration varied most substantially with discharge and sediment flux seasonality (Fig. 6a). The floc

525 volume concentration was ~3 to 5×10^{-4} for the sites in the spring except for site M1, which had a smaller concentration of 2 to 3×10^{-4}. All floc concentrations in the summer were far smaller than the concentrations in the spring at ~5 to 8×10^{-5}. The median floc diameter, $D_{f,50}$ (m), was ~50 to 90 μm for the channel sites and ~35 μm for the island sites with little vertical variation (Fig. 6b). The floc and raw LISST results are similar because flocs composed most of the particle volume concentration. This is evident from the fact that the floc concentration far exceeds the primary particle concentration (order 530 10^{-4} versus 10^{-5}, respectively), implying the floc bulk solid fraction was ~0.1, which is typical for highly porous natural flocs (McCave, 1984; Gibbs, 1985; Eq. 2). We revisit the solid fraction in Sect. 5.7. The depth-averaged floc size distributions at the channel sites were similar for spring and summer. In contrast, the floc size distributions at the two island sites were skewed toward finer flocs (Fig. 6c). Almost all flocs were smaller than the depth-averaged Kolmogorov microscale (Fig. 6d), a result consistent with the idea that the Kolmogorov microscale sets the maximum floc size (Van Leussen, 1988; Kuprenas 535 et al., 2018).
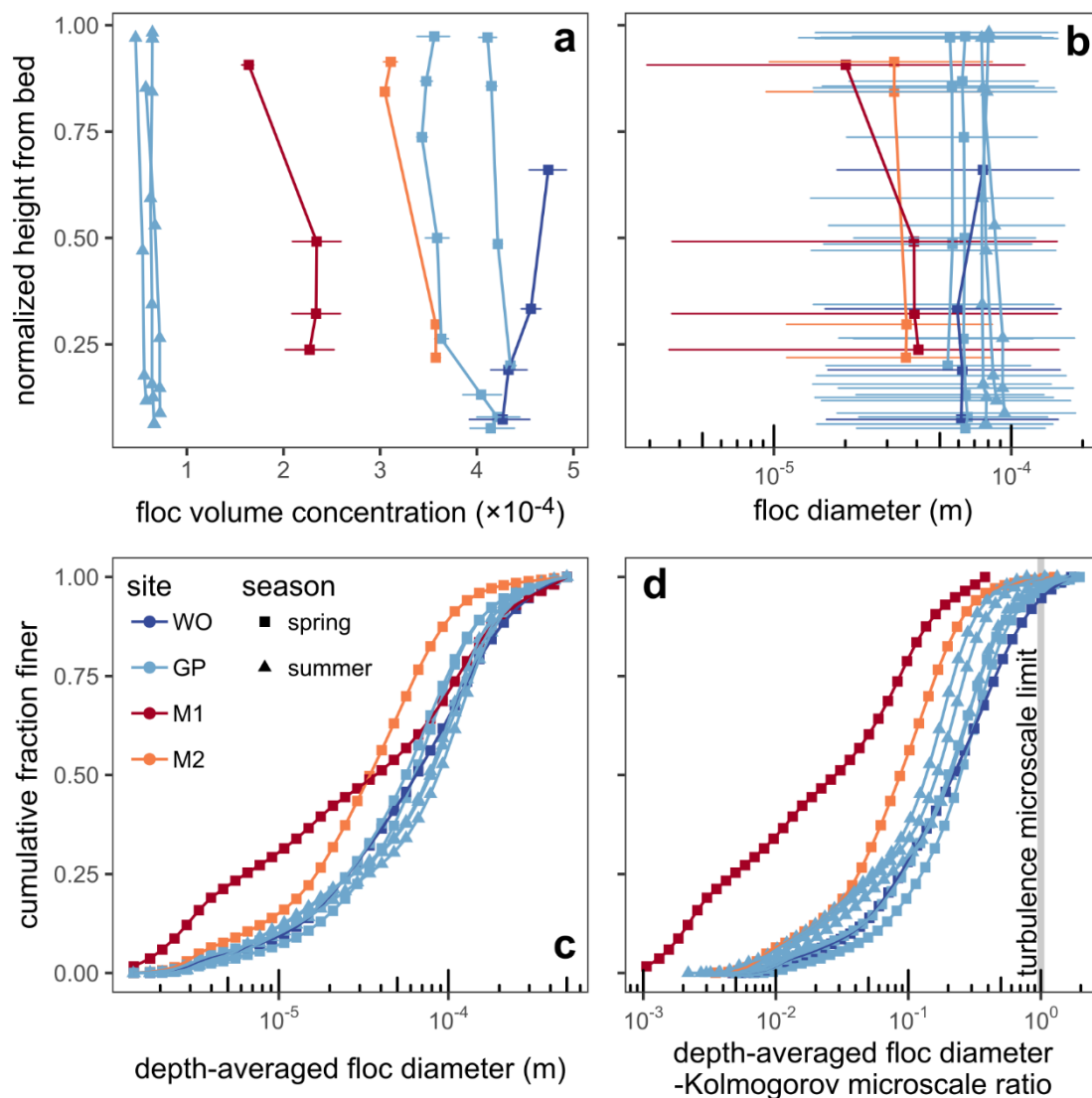
Figure 6: Floc volume concentration and diameter results. (a) Profiles of floc volume concentration. Horizontal bars represent the 95% bootstrap uncertainty. (b) Profiles of floc diameter. Points represent the median floc diameter. Horizontal bars represent the span of the D_{16} and D_{84} floc diameters. (c) Cumulative distribution functions of depth-averaged floc diameter. (d) Cumulative distribution functions of the ratio of depth-averaged floc diameter and Kolmogorov microscale. The legend in panel c applies for all panels.

5.6 Fractal dimension and effective primary particle diameter

Next, we derived two key parameters of the explicit model, fractal dimension, n_f, and effective primary particle diameter, D_p, using the floc size distribution and bulk solid fraction (Sect. 5.5; Table 1). We computed n_f and D_p to ensure consistency

between the mean floc settling velocity and bulk solid fraction under fractal theory across the floc size distribution (Sect. 4.5.2; Table 1).

The fitted fractal dimension is narrowly constrained to ~2 to 2.15, which is well within the expected range of 1.7 to 2.3 for natural flocs (Fig. 7a; Tambo and Watanabe, 1979; Winterwerp, 1998). We deemed $n_f = 2.1$ to be representative for

550   WLD flocs. Fractal dimension correlates strongly with median floc diameter despite the small range of fractal dimension (Fig. 7a), but the reason for the correlation is unclear. Some studies proposed that fractal dimension decreases with the ratio of floc and primary particle diameters, $D_{f,50}/D_{p,50}$ (Khelifa and Hill, 2006; Maggi et al., 2007; Kumar et al., 2010). In contrast, we found that the fractal dimension increases with $D_{f,50}/D_{p,50}$ according to a small, albeit statistically significant, power (p-value = 8.7×10^{-5}; Fig. 7b). Smaller n_f in the island compared to that in the channel might indicate floc restructuring

555   in response to changes in factors like turbulence, sediment concentration, organic matter, and water chemistry.
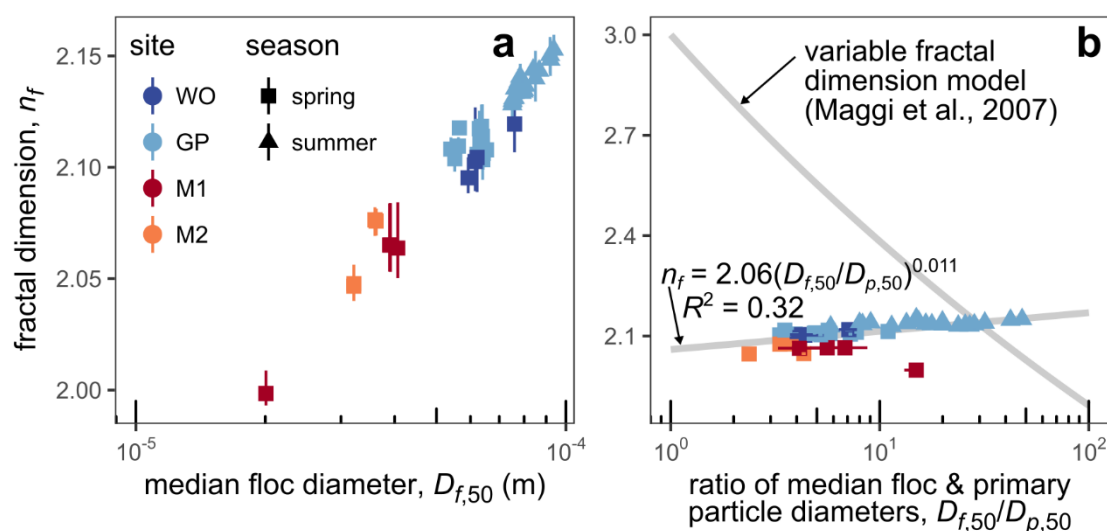
Figure 7: Fractal dimension results. (a) Fractal dimension and median floc diameter. Horizontal and vertical bars represent the 95% bootstrap uncertainty. Bars are smaller than the points where they are not visible. (b) Ratio of median floc and primary

560   **particle diameters and fractal dimension. We used the median primary particle diameter, $D_{p,50}$, not the fitted effective primary particle diameter for consistency with past studies. Horizontal and vertical bars represent the 95% bootstrap uncertainty.**

We tested two models for the effective primary particle diameter, D_p: (1) the fractal model (Eq. 3 and 11) and (2) the median primary particle diameter, $D_{p,50}$. The fitted effective primary particle diameter is tightly constrained to ~2 μm with a range of

565   ~1 to 3 μm (Fig. 8). To predict D_p, the full fractal model (Eq. 3; Bushell and Amal, 1998) requires knowledge of all primary particle diameters within a floc. We simulated them by random draws from the primary particle size distribution (Sect. 4.5.3). The good agreement between the simulated and measured median primary particle diameter validates the simulation

method (Fig. A2a). Alternatively, the fractal model can be simplified to depend directly on moments of the primary particle

size distribution (Eq. 11). We used the simple form (Eq. 11) as the fractal model because it yields very similar predictions to

570 the simulation results of the full model (Fig. A2b). The fitted primary particle diameters are about a factor of 2 on average

(and up to a factor of 6) smaller than the median, indicating that the median is a poor representation of the effective primary

particle diameter (Fig. 8a). The fractal model better predicts the effective primary particle diameter (Fig. 8b), supporting the

hypothesis that, in the case of many primary particle sizes, D_p should be specified to satisfy fractal constraints. However, the

fractal model still overestimates D_p by a factor of about 2-3 in some cases. Potential error in converting a volume-based size

575 distribution to a number-based distribution might be responsible for the misfit. Nevertheless, the fractal model predicts a

range more representative of the effective primary particle estimates than the median (Fig. 8c). If one assumed D_p is the

median, then one would overestimate the solid fraction and floc settling velocity by a factor dependent on the fractal

dimension (Eq. 1 and 2). In our data, this overestimation factor ranges from 1 (no effect) to 5 and has a median of 2.2 (Fig.

8d).

580
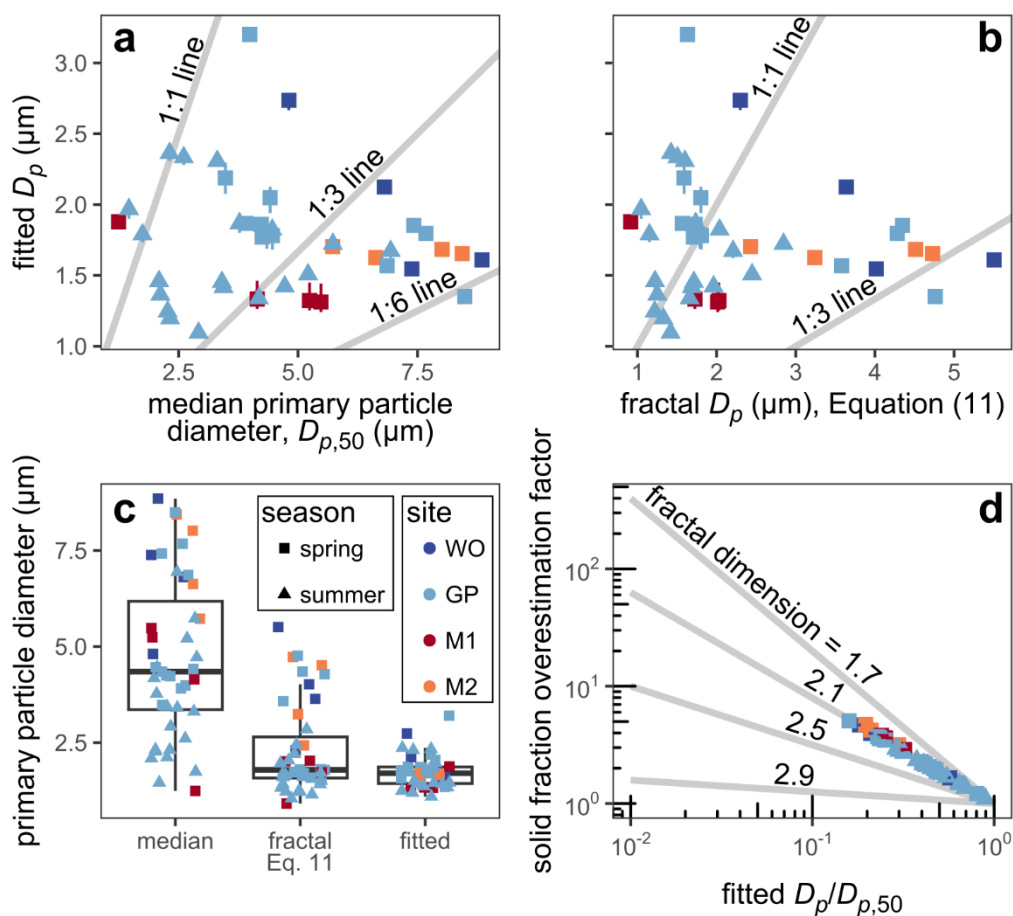
Figure 8: Effective primary particle diameter, D_p, results from primary particle size distributions (Sect. 4.5.1), fitted D_p (Sect. 4.5.2), and the fractal D_p model (Sect. 4.5.3). (a) Median primary particle diameter and fitted effective primary particle diameter. Vertical bars indicate the 95% bootstrap uncertainty on the fitted effective primary particle diameter. (b) Fractal (Eq. 11) and fitted effective primary particle diameters. (c) Boxplots of primary particle diameters. For each boxplot, the lower, central, and upper hinges indicate the 25, 50, and 75th percentiles, respectively. (d) Ratio of fitted effective and median primary particle diameters and the solid fraction overestimation factor. The lines represent contours of constant fractal dimension. The legend in panel c applies to all panels.

5.7 Drag ratio, floc solid fraction, and settling velocity distribution

We estimated the final unknown in the explicit model, the drag ratio, Ω, as the ratio of the explicit model settling velocity (with fitted n_f, D_p, and $\Omega = 1$) and floc cam-measured settling velocity (Sect. 4.5.2; Table 1) and evaluated the values against floc permeability theory. The best-fit constant Ω is 0.51 with lower and upper error estimates of 0.39 and 0.71, respectively, indicating substantial floc drag force reduction due to permeability (Fig. 9a).

We compared drag ratio estimates initially to two models, the Brinkman model (Eq. 4) and the Li and Logan modification of the Brinkman model. The Brinkman model, which assumes uniform porosity and a single primary particle size, is incompatible with the data because ~92% of the data (excluding $\Omega > 1$ data) lie below the predicted minimum Ω (i.e., maximum permeability) for the given n_f (Fig. 9a). The Li and Logan variant (Sect. 2.1), which uses a larger cluster diameter, D_c, in place of the effective primary particle diameter, also cannot explain the data because replacing D_p with D_c does not alter Brinkman's minimum Ω, which is solely a function of n_f. Instead, we propose a new empirical "permeable cluster model," in which we preserve the original solid fraction in the Brinkman model (unlike Li and Logan), but use D_c instead of D_p in the diameter ratio term (like Li and Logan). The model is so named because it implies that the clusters are themselves permeable (Sect. 6.2). We calculated D_c for each drag ratio estimate to test the permeable cluster model. Differences in the cluster diameter can explain the full variability in the relationship between the solid fraction and drag ratio (Fig. 9b). In contrast, the Brinkman model, setting fractal dimension to 2.1, predicts drag ratio very close to 1 (impermeable floc) across all solid fractions and is inconsistent with the data. The ratio of cluster and floc diameters, D_c/D_f, has a median of 0.11 and 16th and 84th percentiles of 0.047 and 0.22. However, the permeable cluster model is limited because we could not determine how to predict D_c.
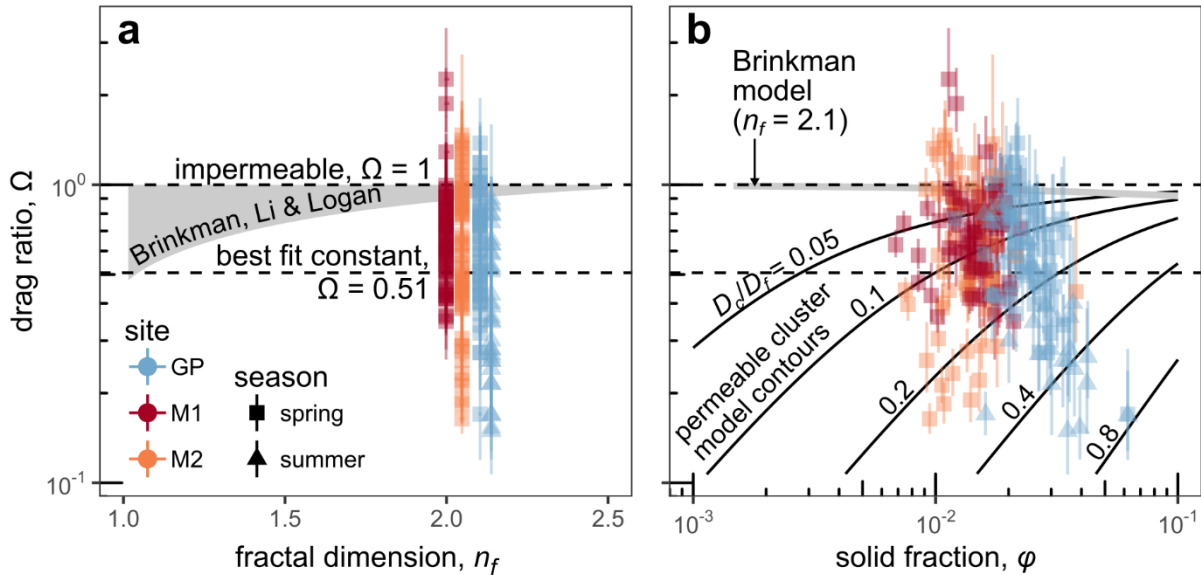
Figure 9: Drag ratio, Ω, results from combining the explicit model and floc settling velocity measured from floc cam images. (a)
Fractal dimension and drag ratio. The shaded area indicates the field of all possible Ω under the Brinkman model (Eq. 4) and the
Li and Logan modification. (b) Solid fraction and drag ratio. The black curves are contours of the permeable cluster model at
different values of cluster-floc diameter ratio, D_c/D_f. Vertical bars indicate the propagated 95% confidence interval of floc cam-
measured settling velocity.

Turning to the remaining floc properties, the bulk solid fraction and settling velocity ranged from ~0.05 to 0.15 (excepting higher fractions at site M1; Fig. 10a) and ~0.1 to 1 mm s^{-1} (Fig. 10b), respectively, and once again varied little in the vertical (Fig. 10ab). The bulk solid fractions are in line with prior floc density measurements (e.g., Van Leussen, 1988). We applied the fitted n_f, D_p, and Ω = 0.51 in the explicit model to calculate floc settling velocity distributions from the floc size distributions (Sect. 4.5.2). We used a constant Ω for simplicity because we could not predict cluster diameter. The median floc settling velocities at the channel sites in spring and summer were ~0.2-0.5 mm s^{-1} (Fig. 10bc). The island sites had median floc settling velocities of about 0.1 mm s^{-1}, with a substantial fraction of floc settling velocity of order 0.01 mm s^{-1}. The smaller fractal dimension and finer floc size distribution in the island caused slower floc settling velocity in the island compared to that in the channels (Fig. 6; Fig. 7).
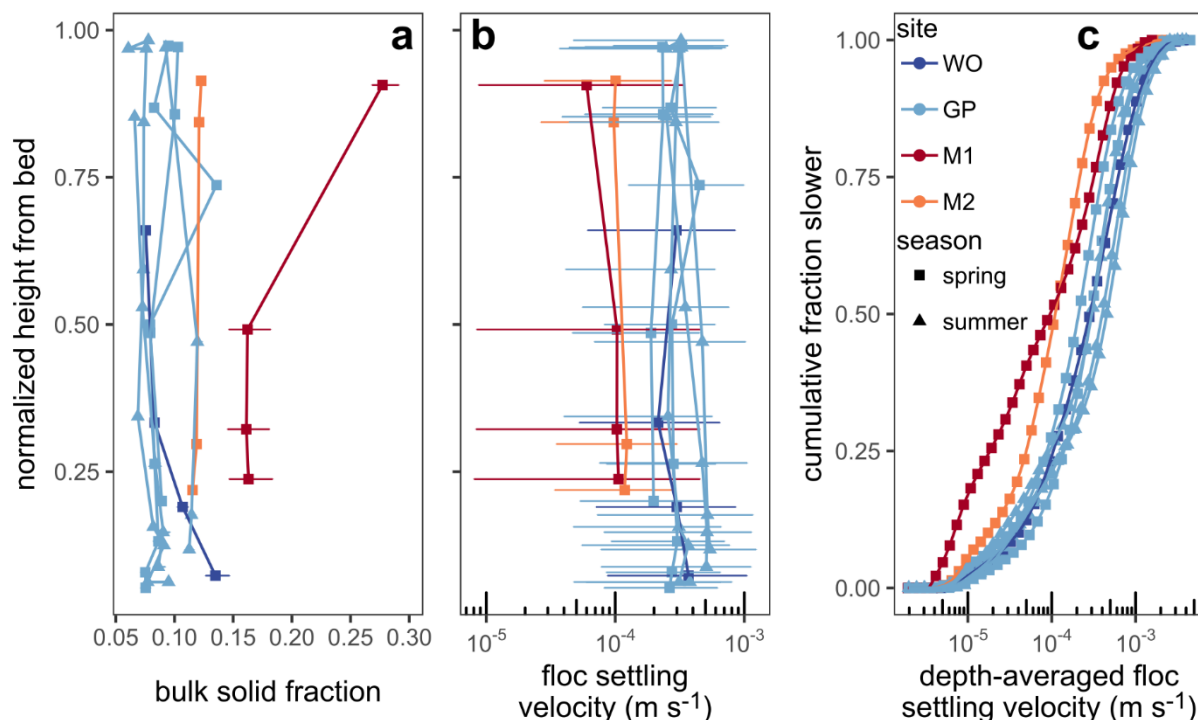
Figure 10: Floc bulk solid fraction and settling velocity results. (a) Profiles of bulk solid fraction. Horizontal bars represent the 95% bootstrap uncertainty. (b) Profiles of floc settling velocity. Points represent the median floc settling velocity. Horizontal bars represent the span of the 0.16 and 0.84 quantile floc settling velocities. (c) Cumulative distribution functions of depth-averaged floc settling velocity. The legend in panel c applies for all panels.

Flocculation ultimately caused an order 10- to 100-fold increase in in situ diameter and settling velocity compared to those of primary particles according to the distribution quantiles (Fig. 11). The floc diameter quantile is systematically larger than the corresponding primary particle quantile for all profiles by a typical factor of 10 (Fig. 11a). The median floc diameter is at least 4 times greater than the median primary particle diameter for all profiles and at least 10 times for five profiles. The floc settling velocity quantile relative to the primary particle settling velocity quantile is distributed across a wide range of factors from ~1, for the coarsest fractions of the primary particle distribution, to >100, for the finest fractions of the primary particle distribution (Fig. 11b). This pattern shows that flocculation more strongly enhanced the settling velocity of fine grains than that of coarser (but still flocculated) grains because the settling velocities of the coarsest flocculated grains approach the floc settling velocity (Lamb et al., 2020; Nghiem et al., 2022). On average, the floc settling velocity quantiles are one order of magnitude faster than the corresponding primary particle settling velocity quantiles.
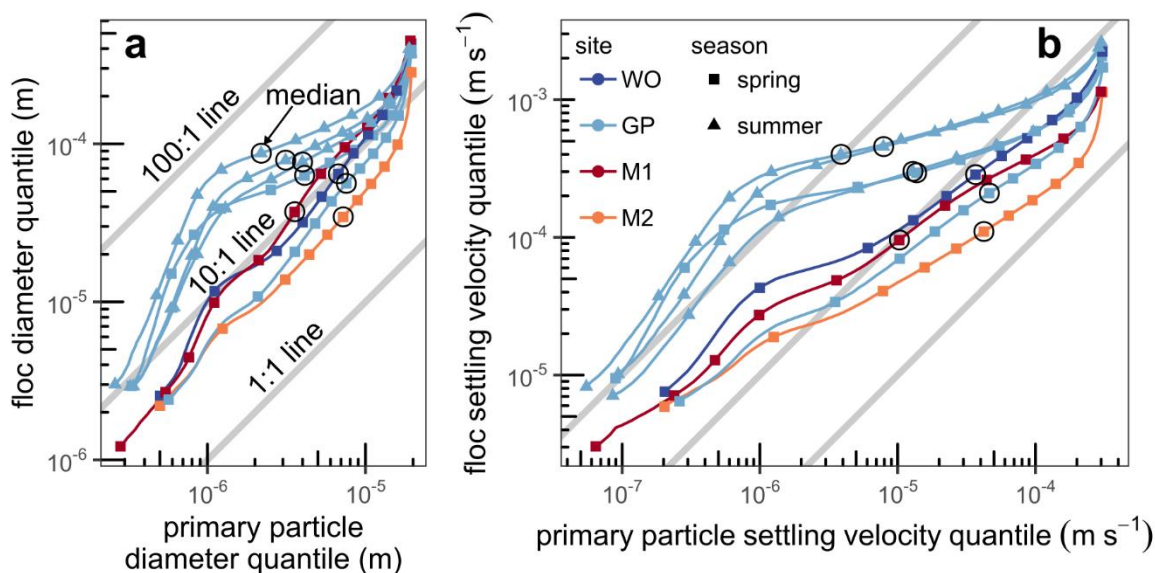
Figure 11: Floc and primary particle quantile-quantile plots for the depth-averaged profiles. (a) Floc and primary particle diameters. 100:1, 10:1, and 1:1 lines are displayed for reference. The median for each profile is circled. (b) Floc and primary
645 **particle settling velocities. The annotations in panel a also apply to panel b. The legend in panel b also applies to panel a.**

Finally, we summarize the relationships between the bulk floc properties (diameter, solid fraction, and settling velocity) measured in WLD. Floc diameter decreased with primary particle diameter for channel sites (Fig. 12a). No trend is apparent for the island sites. There is little correlation between bulk solid fraction and primary particle diameter (Fig. 12b). The
650 relationship between floc settling velocity and primary particle diameter (Fig. 12c) resembles the relationship between floc and primary particle diameters (Fig. 12a). Floc diameter and bulk solid fraction scale inversely as expected from fractal theory (Fig. 12d; Eq. 4), indicating a fractal dimension of 2.4 which is close to the fitted global value of 2.1 (Sect. 5.6). Floc settling velocity also scales inversely with bulk solid fraction (Fig. 12e) as predicted by the explicit model. The floc diameter and settling velocity scale well with each other as expected (Fig. 12f) because we calculated floc settling velocity following
655 the explicit model. In the channels, median floc diameter in the summer tended to be slightly larger (~80 versus ~60 µm) than that in the spring (Fig. 12d). However, the seasonal difference in floc settling velocity is negligible (Fig. 12f) because solid fraction decreases with floc diameter and partly compensates for the diameter difference.
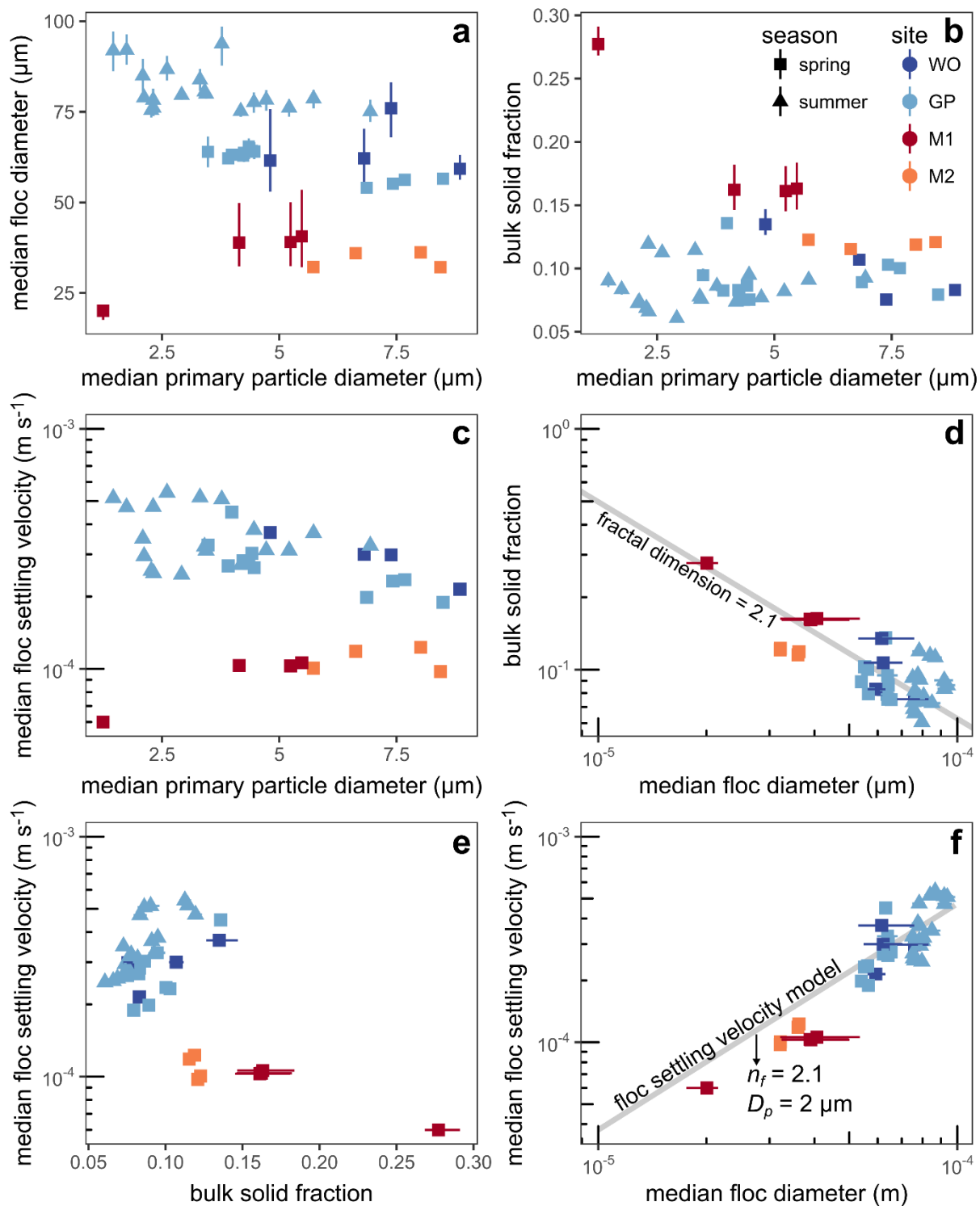
Figure 12: Bulk floc property results. (a) Median primary particle and floc diameters. (b) Median primary particle diameter and bulk solid fraction. (c) Median primary particle diameter and floc settling velocity. (d) Median floc diameter and bulk solid fraction. The line indicates a fractal dimension of 2.4. (e) Bulk solid fraction and median floc settling velocity. (f) Median floc diameter and settling velocity. The line indicates a floc settling velocity model using typical values of the constrained parameters: fractal dimension of 2, an effective primary particle diameter of 2 μm, $b_1 = 10.14$, and $\Omega = 0.51$. The legend in panel b applies for all panels. Horizontal and vertical bars indicate the 95% bootstrap uncertainty.

5.8 Validating explicit model parameters

We compared the floc settling velocities of the Rouse-Vanoni equation inversion method and explicit model as a holistic test of the plausibility of the estimated n_f, D_p, and Ω because these settling velocity estimates are independent. Since the Rouse-estimated settling velocity depends on the choice of floc diffusivity ratio, β_{fl}, (Sect. 4.4), we used three diffusivity ratio models to test sensitivity assuming that they apply to flocs: constant ($\beta_{fl} = 1$), the quadratic equation of Van Rijn (1984), and the empirical best-fit one-parameter equation of De Leeuw et al. (2020). The Van Rijn and De Leeuw models are functions of the ratio of settling and shear velocities. The constant and Van Rijn diffusivity ratio models cause the Rouse-estimated floc settling velocity to be systematically larger than median depth-averaged floc settling velocity from the floc settling velocity distributions ranging from equal to a factor of ~30 faster (Fig. 13). The De Leeuw model yields Rouse-estimated floc settling velocities slower and faster than the median, but the average across all data points indicates approximately equal settling velocities (Fig. 13). The large scatter reflects uncertainty in predicting the diffusivity ratio and that the range of diffusivity ratio is unrestricted in the De Leeuw equation (De Leeuw et al., 2020). In contrast, the diffusivity ratio must be greater than or equal to 1 in the Van Rijn equation and is prescribed to be 1 in the constant case. Although the constant and Van Rijn models suggest that the floc settling velocity of the explicit model might be biased low, we judged that the estimated n_f, D_p, and Ω in the explicit model are reliable because of the favorable comparison to the De Leeuw model, which is based on a large global river data compilation.
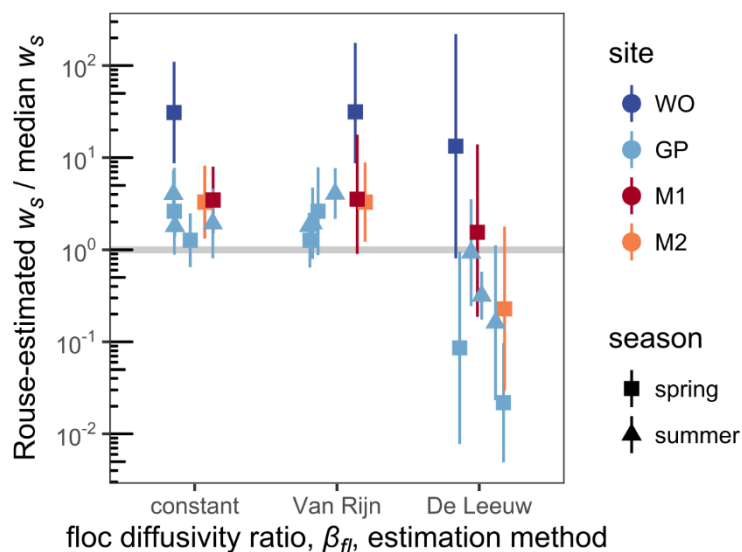
Figure 13: Ratio of Rouse-estimated and median floc settling velocities by floc diffusivity ratio estimation method. The median floc
685 **settling velocity is the median of the depth-averaged floc settling velocity distribution (Fig. 10). Vertical bars indicate the 95%**
confidence interval on shear velocity and standard deviation of Rouse-estimated floc settling velocity with $\beta_{fl} = 1$.

5.9 Semi-empirical model controls on floc properties

The previous sections focused on constraining floc parameters and testing theory for the explicit model. We use the direct
floc measurements to validate the semi-empirical model, in which all parameters are known through geochemical
690 measurements (Sect. 4.6) and calculations in the prior sections, and use the model to examine environmental controls on
flocs in WLD. We compared the semi-empirical model predictions (Eq. 6; Nghiem et al., 2022) and the observed floc cutoff
diameter (sediment concentration-depth profiles, Rouse-Vanoni theory), floc settling velocity (floc cam, LISST combined
with sample data), and floc diameter (LISST combined with sample data). The semi-empirical model predicts the floc cutoff
diameter well within a factor of ~2 of measurements and capture the overall data trend (Fig. 14a). As a note, the measured
695 floc cutoff diameter is not simply equal to 20 µm because the extra profiles without LISST and floc cam data have varying
floc cutoff diameters from 20 to 50 µm. The semi-empirical model floc settling velocity and the fully calibrated floc settling
velocity of the explicit model (indicated as the LISST data points) agree well (Fig. 14b). The floc settling velocities from the
floc cam have inherent variability at the individual floc scale, but the median shows good agreement with the semi-empirical
model within a factor of 2 (Sect. 5.7). The floc diameter results indicate that the semi-empirical model predicts adequately
700 within a factor of ~2, albeit with a limited number of data points (Fig. 14c). The fact that the floc cutoff diameter model
performs the best is expected because it required the fewest assumptions to derive (Nghiem et al., 2022). Overall, the
reasonable performance of the semi-empirical model against direct measurements in WLD validates the model for predicting

floc properties in freshwater. Additionally, the good agreement between the semi-empirical and explicit floc settling velocity models confirms that they are consistent with each other (Fig. 14b).
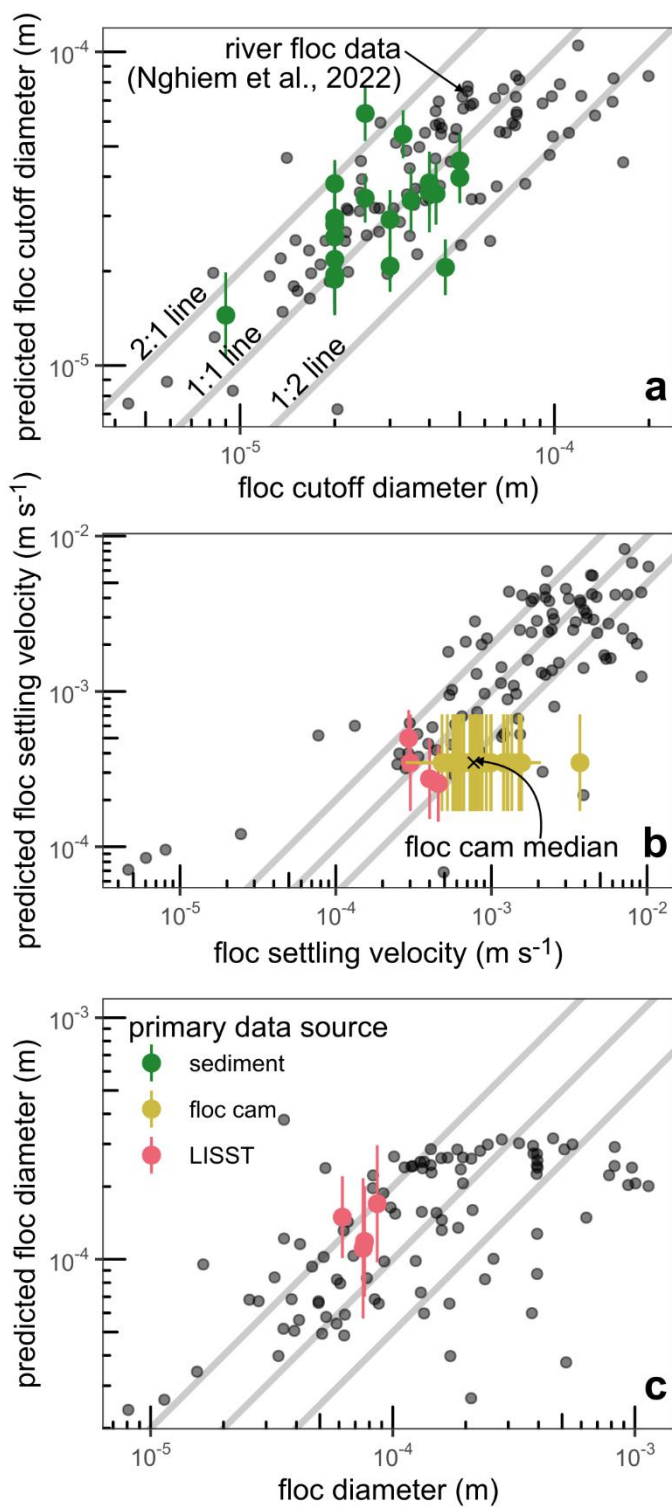
Figure 14: Measured floc properties and predictions of (a) floc cutoff diameter, (b) floc settling velocity, and (c) floc diameter colored by primary data source (Table 1). Black points are data from Nghiem et al. (2022) that were used to calibrate the semi-empirical model. Vertical bars represent the 95% confidence interval of predictions. The labels and legend in panels a and c, respectively, apply to all panels. Sediment data include data from profiles without paired LISST and floc cam data. The floc cam data have the same predicted floc settling velocity because they represent a single floc cam deployment. Data for which water chemistry was not measured are omitted because they lack semi-empirical model predictions, which explains the absence of floc cam data in panel c.

The agreement between the semi-empirical model and floc properties shows that turbulence, sediment concentration and mineralogy, organic matter, and water chemistry control flocculation in WLD (Eq. 6; Nghiem et al., 2022). We plotted the predictors in the semi-empirical model against the floc cutoff diameter, normalized to remove the effects of other variables and by the median, because the floc cutoff diameter model (Eq. 6a) displays the best correlation with measurements (Fig. 14). We expect similar patterns for floc settling velocity and diameter because the floc variables correlate with each other. Turbulence, through the Kolmogorov microscale, limits floc size and settling velocity (Fig. 15a) because the semi-empirical model assumes that floc growth and breakage rates are balanced (Fig. 6d). As median primary particle diameter increases, coarser and faster settling grains can be added to flocs (Fig. 15b). Higher sediment concentration enhances flocculation by increasing particle collision rate (Fig. 15c). The effect of organic matter, as quantified by the organic cover fraction, θ, promotes flocculation at low values, but is predicted to have an opposite effect once $\theta > 0.5$ because high organic coverage stabilizes sediment surfaces from aggregation (Fig. 15d). Sediment Al/Si and relative charge density, Φ, vary inversely with floc properties because they might preferentially cause clay flocculation and exclude faster settling silt grains from flocs (Fig. 15ef). We detected little systematic variation in floc cutoff diameter with season and location in channel or island.
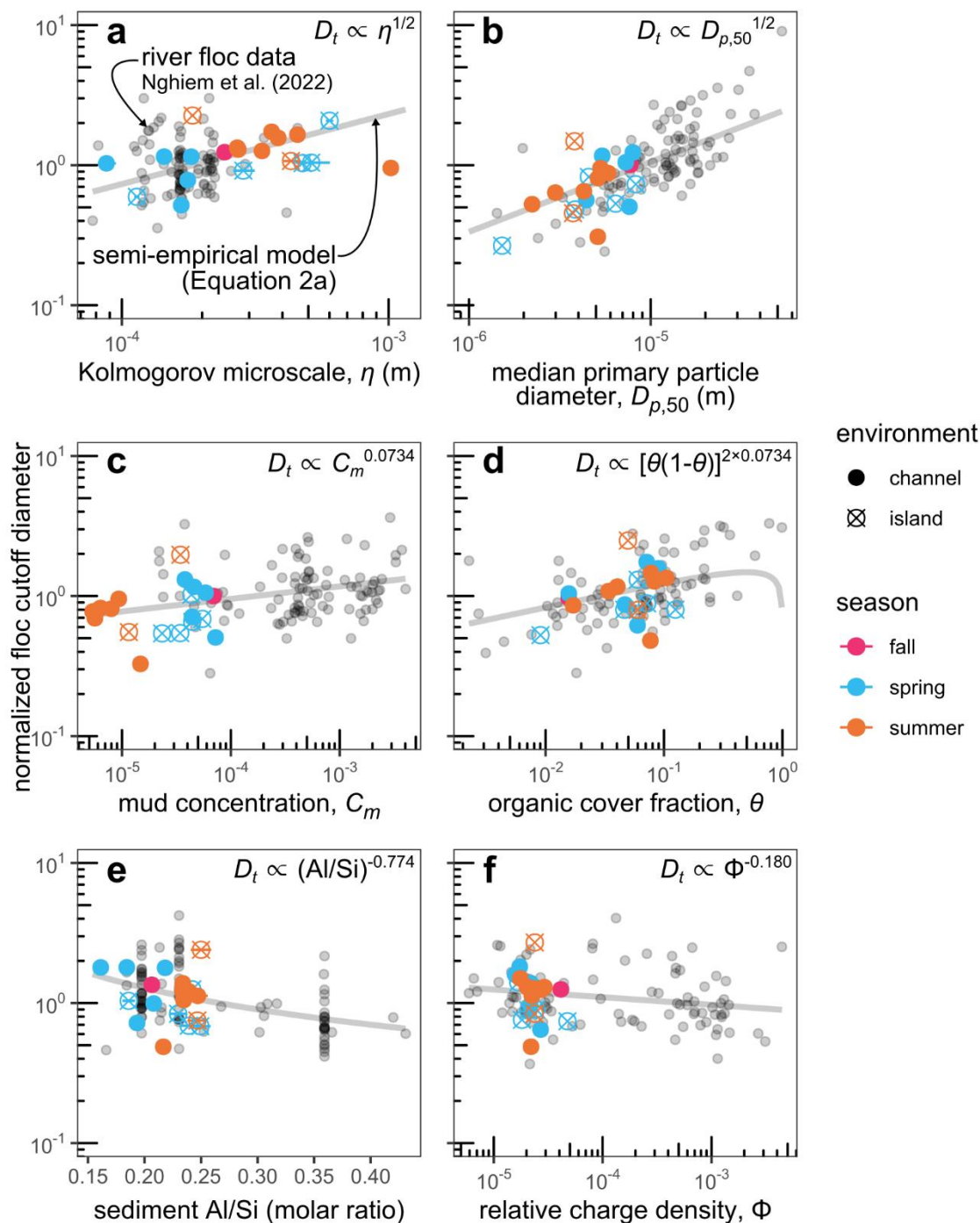
Figure 15: Semi-empirical model predictors plotted against floc cutoff diameter, D_t, normalized by the effects of all other predictors in the floc model (Eq. 6a). Gray curves indicate the model prediction. Horizontal error bars indicate the (a) 95%

730

confidence interval on shear velocity, (d) 1-σ error on percent weight organic carbon, or (e) 95% confidence interval on Al/Si estimates. The labels in panel a apply to all panels.

Trends in Kolmogorov microscale, primary particle diameter, and mud concentration indicate the potential importance of turbulence in reducing the variability of floc characteristics in delta channels. The Kolmogorov microscale correlates with finer median primary particle diameter and higher Al/Si because more turbulent flows (smaller microscale) entrain and suspend coarser sediment (Fig. 16ab). Higher mud concentration in channels corresponds to smaller Kolmogorov microscale because higher fluid stress entrains more sediment from the bed (Fig. 16c). These feedbacks show that finer primary particles, larger Al/Si, and smaller mud concentration (corresponding to smaller floc cutoff diameter) offset the effect of larger Kolmogorov microscale on increasing floc cutoff diameter and ultimately limit variability in floc cutoff diameter in delta channels. The pattern does not hold in the island where the predictors are uncorrelated with Kolmogorov microscale. The remaining variables, organic cover fraction and relative charge density, do not show clear trends by season and location (Fig. 15ef).
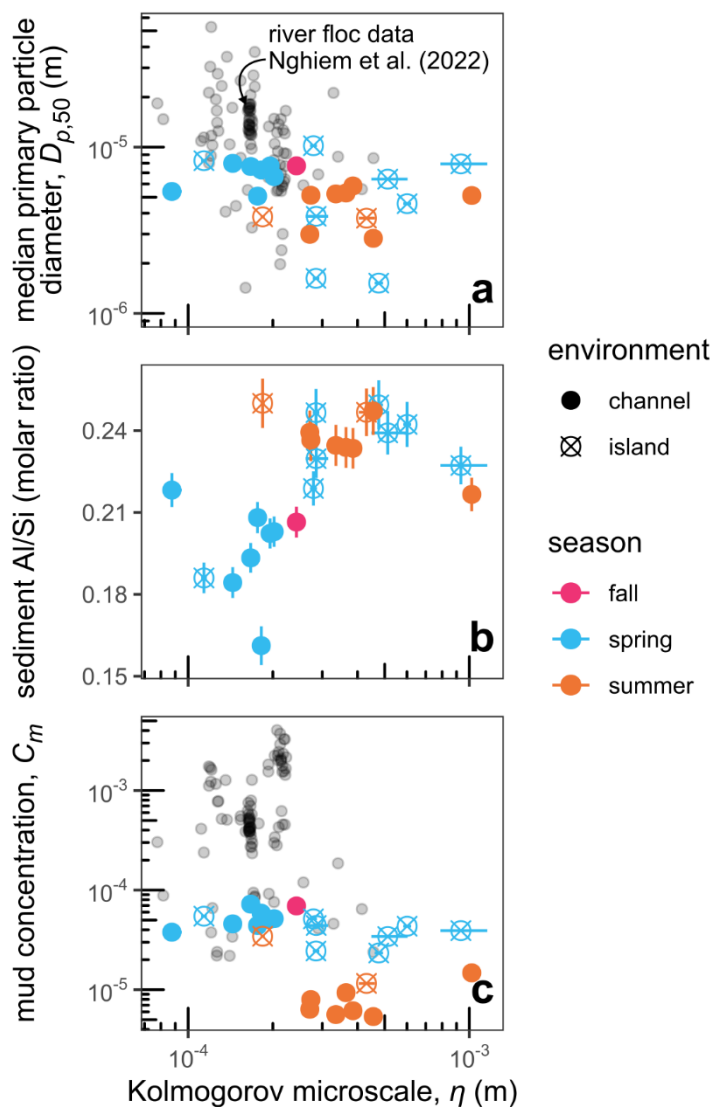
Figure 16: Kolmogorov microscale and (a) median primary particle diameter, (b) sediment Al/Si, and (c) mud volume concentration. Horizontal error bars indicate the 95% confidence interval on shear velocity. In panel b, vertical error bars indicate the 95% confidence interval on Al/Si estimates. River floc data are omitted in panel b because most Al/Si data were compiled from separate data sources in Nghiem et al. (2022).

6 Discussion

6.1 Predicting Floc Settling Velocity

The explicit and semi-empirical floc settling velocity models yield consistent predictions (Fig. 14b), suggesting that, in practice, the model choice depends on data availability. The explicit model has conventionally been used to predict the floc settling velocity given the floc diameter, but suffered from uncertainty in the effective primary particle diameter and drag ratio. Although we used joint camera, in situ particle sizing, and suspended sediment concentration and grain size distribution profiles to constrain effective primary particle diameter and drag ratio, we suggest that the explicit model can still be used to predict floc settling velocity given only suspended sediment grain size distribution and floc diameter (e.g., through camera or in situ particle sizing data). The primary particle size distribution can be obtained from the suspended sediment grain size distribution by choosing a floc cutoff diameter (in the range of ~20 to 50 μm; Nghiem et al., 2022) and removing coarser sediment from the distribution. The fractal dimension of natural flocs can be assumed to be 2 (Winterwerp, 1998). The fractal dimension and primary particle size distribution feed into the simplified fractal model (Eq. 11) to predict effective primary particle diameter. Predicting drag ratio remains a challenge because prior analytical permeability models perform poorly for WLD flocs (Fig. 9). Although a new permeable cluster model can capture the full range of drag ratios (Fig. 9b), it is difficult to use because a model for cluster diameter is missing. For simplicity, Ω can be assumed to be an appropriate constant based on field measurements or the values reported here.

The semi-empirical model has the advantage of relying on geochemical factors that can be easier to estimate, especially as functions of space and time, compared to the floc parameters in the explicit model. The consistency between the models indicates that the effects of D_p and Ω are implicitly captured in the semi-empirical model. The full unsteady form of the semi-empirical model, along with a host of other existing dynamic models (e.g., Xu et al., 2008; Son and Hsu, 2011; Shen et al., 2018), can be used to predict floc settling velocity through time and space in a sediment transport model. However, this approach can be computationally expensive and require parameters that are difficult to constrain. Our analysis suggests the assumption of local equilibrium is a reasonable simplification to predict floc properties because our observations are consistent with the equilibrium semi-empirical model (Fig. 14). This fact implies that flocs quickly adjust to their local conditions, a behavior that has some experimental evidence (Tran et al., 2018). We suggest that an even simpler treatment, using a single constant floc settling velocity for the mud settling velocity as is common in sediment transport models (Roberts et al., 2000; Braat et al., 2017), is reasonable in alluvial channels because tradeoffs between turbulence and primary particle size and mineralogy can compensate for each other and limit the variability in floc settling velocity (Sect. 5.9 and 6.3).

6.2 Role of effective primary particle diameter and drag ratio on floc settling velocity

Our results indicate that the effective primary particle diameter should be calculated using a fractal equation that conserves the volume and fractal space of the original primary particles (Bushell and Amal, 1998; Eq. 3 and 11; Fig. 8) in contrast to

past work that treated D_p as a characteristic length scale of primary particles (Syvitski et al., 1995; Strom and Keyvani, 2011). The median primary particle diameter tends to overestimate the effective primary particle diameter, solid fraction, and floc settling velocity (Fig. 8d). The simplified fractal equation (Eq. 11) is suitable to predict D_p given the number-based
785   primary particle size distribution because flocs contain sufficiently many primary particles for the central limit theorem to hold (Fig. A2b). We expect the fractal model to also hold in saline environments.

A new permeable cluster model explains our drag ratio estimates better than the Brinkman model likely because it empirically allows for clusters to be permeable. In the Brinkman model, flow through the floc is assumed to impart drag on the primary particles (Brinkman, 1947). By using a larger cluster diameter instead of primary particle diameter, the Li and
790   Logan variant causes a relatively small increase in permeability because the increase in solid fraction partially offsets the effect of larger pores caused by reorganization of primary particles into clusters (Kim and Stolzenbach, 2002). The permeable cluster model is essentially a middle ground because, like the Li and Logan model, it uses a cluster diameter relative to the floc diameter as the key length scale in the permeability equation (e.g., Eq. 4). However, like the Brinkman model, it uses the original solid fraction and hence assumes primary particles are subject to the drag, a behavior that implies
795   that the clusters themselves are permeable because primary particles are still able to experience the flow.

On the other hand, the classic Brinkman model underestimates floc settling velocity and floc permeability (i.e., overestimates drag ratio) in our data because one or both assumptions of uniform porosity and single primary particle size are violated. Although typical permeability equations have the same assumptions, a different permeability equation among the many available (see review in Kim and Stolzenbach, 2002) might be consistent with the drag ratio estimates. Indeed,
800   Kim and Stolzenbach (2002) found that many models, including Brinkman, underestimated the permeability of fractal aggregates (albeit with a single primary particle diameter), but the Davies (1953) model performed well. However, we found that the Davies model likewise is not compatible with our drag ratio estimates using the same analysis as in Sect. 5.7. If fractal structure is not the source of the discrepancy, then the presence of multiple primary particle sizes might be responsible because it can control the pore size and structure distribution (e.g., Li and Logan, 2001; Kim and Stolzenbach,
805   2002). In addition, the configuration of organic matter within flocs might also affect permeability by controlling flow paths. Clearly, it is difficult to account for all these effects using a general theory because the complete floc structure and composition must be known. The cluster diameter in the permeable cluster model empirically encapsulates the combination of these effects, making it difficult to link the cluster diameter to a physical measurement.

Although the drag ratio estimates depend on the assumed floc shape, floc shape is not responsible for the inability
810   of the Brinkman model and the Li and Logan method to reproduce the observed drag ratios. Floc shape affects the shape factor, b_1, in the explicit model. Larger values of b_1 cause smaller drag ratio estimates (Sect. 4.5.2). Stokes law shows that $b_1 = 18$ (Stokes, 1851) for an impermeable sphere ($\Omega = 1$), so $b_1 = 20$ is commonly assumed as done here because natural particles are not perfect spheres (Ferguson and Church, 2004). Strom and Keyvani (2011) suggested that $b_1 \sim 20$ is suitable for flocs with $n_f < 2$, but $b_1 = 120$ for flocs with $n_f \geq 2.5$. Regardless of the precise value of b_1, particle shape effects only
815   cause $b_1 > 18$ because shape irregularities induce more drag and slow the settling velocity (McNown and Malaika, 1950;

Dietrich, 1982). We used a relatively low value of $b_1 = 20$ to calculate the drag ratio, so higher b_1 would only further amplify floc permeability and exacerbate the discrepancy with theory.

6.3 Environmental Controls on Flocculation

We argue that turbulence is the overriding variable controlling flocculation in the distributary channels of WLD because it
820 not only directly affects particle collision rates and floc breakage (Winterwerp, 1998), but also sets concentration and primary particle size and mineralogy (Fig. 16). Sediment entrainment scales nonlinearly with boundary shear velocity and, along with settling and bed grain size distribution, sets the sediment concentration (e.g., García, 2008; De Leeuw et al., 2020). More turbulent flows can source larger primary particles that have distinct mineralogy (via Al/Si) than finer grains. All else equal, these effects correlate to coarser floc cutoff diameter, faster floc settling velocity, and coarser floc diameter
825 (Eq. 6). However, increases in turbulence intensity cause floc breakage at equilibrium, thereby compensating against these. These negative feedbacks demonstrate that flocculation can buffer partially against spatiotemporal changes in turbulence, a mechanism that might explain the limited seasonal floc settling velocity variation of 0.2-0.6 mm s^{-1} in the lower Mississippi River (Osborn et al., 2023) and, more broadly, the limited global variation of 0.1 to 1 mm s^{-1} (e.g., Hill et al., 2000; Mikkelsen et al., 2007; Nghiem et al., 2022). In contrast to flocs in channels, floc predictions in wetlands appear to be more
830 uncertain because, in the islands, Kolmogorov microscale is uncorrelated with primary particle diameter, Al/Si, and mud concentration (Fig. 16). These patterns might be because sediment dynamics are more complicated in these shallow island wetlands where two-dimensional unsteady tidal, wave, and hysteresis effects might be important (Geleynse et al., 2015; Bevington et al., 2017).

In contrast to the other factors, organic cover fraction and relative charge density vary less and are not responsible
835 for the bulk of the variability in floc parameters (Fig. 15). This does not imply that they are unimportant for flocculation. Instead, we propose that they are allogenic catchment-wide controls on flocculation and vary over longer time scales. For example, tectonic activity and climate change can alter biological productivity and chemical weathering intensity on the catchment scale (Geider et al., 2001; West et al., 2005), altering the organic cover fraction and relative charge density through changes in organic carbon loading on sediment and water chemistry (e.g., Galy et al., 2008). The fact that these
840 effects are not directly linked to turbulence feedbacks implies that, despite their longer time scale, they can cause persistent changes in floc properties that are not simultaneously offset. In contrast, Kolmogorov microscale, sediment concentration, Al/Si, and primary particle size vary on shorter flood-to-seasonal discharge time scales. Their effects on flocculation can be considered autogenic because they adjust together to discharge and sediment supply (e.g., Phillips et al., 2022).

7 Conclusion

845 Flocculation controls the transport and distribution of mud across rivers and wetlands by increasing the effective mud settling velocity. Using multiple techniques – a camera, in situ LISST particle size and concentration, and Rouse-Vanoni

concentration-depth profile inversion – we observed flocs in Wax Lake Delta, LA, with median diameters of 30 to 90 μm, bulk solid fraction of 0.05 to 0.3, and settling velocities on the order of 0.1 to 1 mm s^{-1} with little vertical variation. Flocs included silt grains up to 20 to 50 μm in diameter. Flocs in channels tended to be larger and lighter, while flocs in an island wetland tended to be smaller and denser. On average, floc diameter and settling velocity were an order-of-magnitude larger than those of primary particles. We used this data to validate and calibrate an explicit floc settling velocity model based on Stokes law and a semi-empirical model, which relies on hydrodynamic and geochemical data.

We constrained two key unknowns, effective primary particle diameter and drag ratio, in the explicit model. For the first time for natural flocs, we verified a fractal model for effective primary particle diameter that conserves the volume and fractal space of the original primary particles. This result shows that, assuming flocs are fractal aggregates, the effective primary particle diameter is not a simple characteristic length scale like the median as previous studies assumed. The median primary particle diameter systematically overestimates the effective primary particle diameter by an average factor of 2 and up to a factor of 6, leading to overestimates of floc solid fraction and settling velocity. Floc permeability, quantified by the drag ratio, has been little explored for natural flocs. Measured flocs were appreciably permeable, increasing the floc settling velocity by a factor of about 2. The drag ratio estimates do not conform to classic permeability theory because the theory does not consider fractal structure, the primary particle size distribution, and the presence of organic matter. Instead, a new permeability model, in which permeable clusters of primary particles enhance permeability, can explain the estimates using an empirical cluster diameter that absorbs the unknowns.

We also verified the semi-empirical model using floc cutoff diameter, settling velocity, and diameter data and showed that its floc settling velocity predictions are consistent with those of the explicit model. The semi-empirical model reveals that turbulence, sediment concentration and mineralogy, organic matter, and water chemistry control flocculation in WLD and suggests that flocs can be reasonably modeled in local equilibrium. Results emphasize the importance of turbulence feedbacks on sediment concentration, mineralogy, and primary particle diameter for mitigating changes in floc size and settling velocity in alluvial channels on flood and seasonal time scales. Changes in organic matter binding and sediment surface charge interactions might affect flocculation at longer time scales because they are set by allogenic catchment-to-continental scale processes. Overall, the semi-empirical and explicit models are both viable options for predicting floc settling velocity in rivers and freshwater wetlands, but require knowledge of different predictors.

Appendix A

We performed X-ray fluorescence (XRF) analysis to measure sediment Al/Si on two different instruments because of sample mass limitations. We measured the absolute concentrations of Al and Si using the glass pellet fusion method on a 4 kW Zetium Panalytical XRF analyzer for 7 samples and calculated the quantitative Al/Si. However, this method requires ~1 g of sediment, which is larger than the total mass of most of our suspended sediment samples. For 20 samples with less mass, we measured the relative abundances of Al and Si using a Rigaku Primus IV XRF Spectrometer, which directly scans powder

samples, and calculated the semi-quantitative Al/Si using its semi-quantitative package, SQX. We also re-analyzed the
880 samples that had been measured on the Zetium using the Rigaku to calibrate a relationship to convert the semi-quantitative
Al/Si to quantitative Al/Si ($R^2 = 0.91$; Fig. A1a). Next, we developed a linear model between sediment Al/Si and volume
fraction finer than a certain grain size threshold. We tested the model coefficient of determination for many grain size
thresholds (Fig. A1b). We selected a linear model between Al/Si and the volume fraction finer than 19.2 μm (Al/Si =
0.099 + 0.16[fraction finer than 19.2 μm]) because this threshold yielded the highest R^2 of 0.88. We predicted Al/Si from
885 the depth-averaged grain size distributions for all concentration profiles using this grain size relationship.
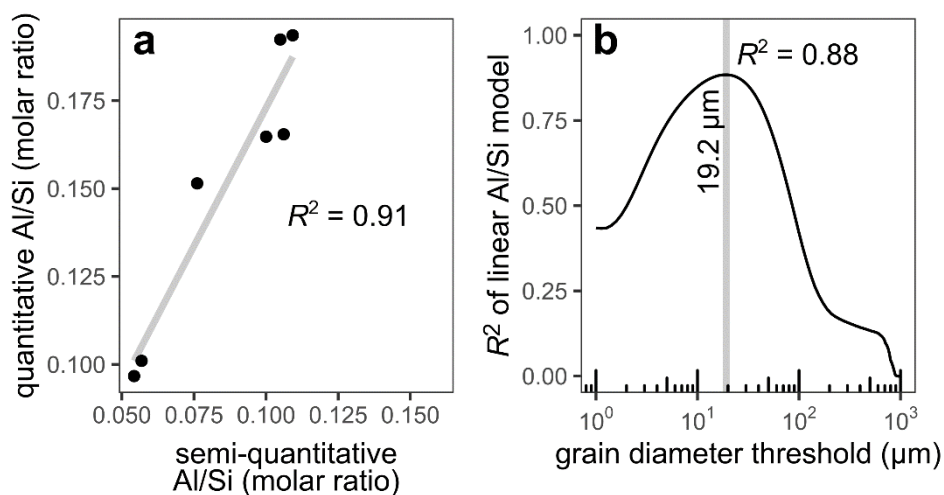
**Figure A1: Sediment Al/Si calibrations. (a) Scatterplot of semi-quantitative Al/Si and quantitative Al/Si. (b) Coefficient of
determination, R^2, of a linear model between Al/Si and volume fraction finer than a grain diameter threshold as a function of the
890 threshold.**
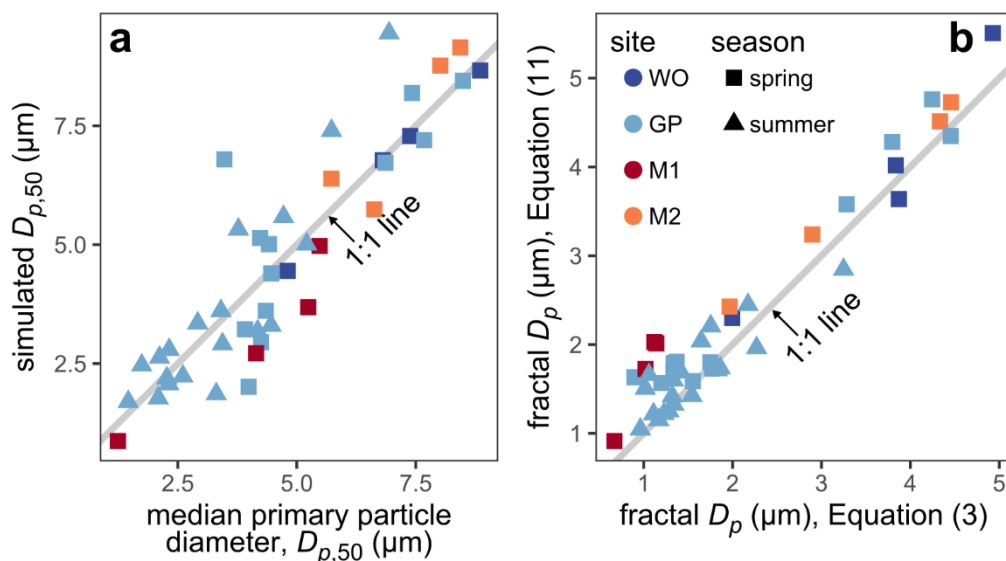
Figure A2: Fractal D_p model validation (Sect. 4.5.3 and 5.6). (a) Measured and simulated median primary particle diameter. Simulations represent random draws from the primary particle size distribution for 10,000 flocs for each data point (Sect. 4.5.3). (b) Fractal effective primary particle diameter using the full (Eq. 3) and simplified equations (Eq. 11). The legend in panel b applies to all panels.

Notation

Al/Si	Sediment Al-Si ratio, molar ratio
b_1	Settling velocity model constant (= 20), dimensionless
C_{fl}	Floc volume concentration, dimensionless
C_i	Sediment volume concentration for ith grain size class, dimensionless
C_{bi}	Near-bed sediment volume concentration for ith grain size class, dimensionless
D_c	Cluster diameter, m
D_f	Floc diameter, m
$D_{f,50}$	Median floc diameter, m
D_p	Effective primary particle diameter, m
$D_{p,50}$	Median primary particle diameter, m
D_t	Floc cutoff diameter, m
g	Gravitational acceleration (= 9.81 m s^{-2}), m s^{-2}
h	Local water depth, m
h_b	Near-bed height (= 0.1h), m

k	Floc permeability, m^2	
n_f	Floc fractal dimension, dimensionless	
p_i	Rouse number for ith grain size class, dimensionless	
915	R_s	Submerged specific gravity of sediment (= 1.65), dimensionless
	u_*	Shear velocity, m s^{-1}
	w_s	Floc settling velocity, m s^{-1}
	w_{si}	In situ particle settling velocity for ith grain size class, m s^{-1}
	β	Sediment diffusivity ratio, dimensionless
920	β_{fl}	Floc diffusivity ratio, dimensionless
	η	Kolmogorov microscale, m
	θ	Organic cover fraction, dimensionless
	κ	Von Kármán constant (= 0.41), dimensionless
	v	Kinematic viscosity of water (= 10^{-6}), m^2 s^{-1}
925	ξ^{-2}	Dimensionless floc permeability, dimensionless
	ρ	Water density (= 1000), kg m^{-3}
	ρ_s	Sediment density (= 2650), kg m^{-3}
	Φ	Relative charge density, dimensionless
	φ	Floc solid fraction, dimensionless
930	$\bar{\varphi}$	Bulk floc solid fraction, dimensionless
	Ω	Drag ratio, dimensionless

Code availability

NA

Data availability

935 NASA Delta-X data are available online at https://daac.ornl.gov/cgi-bin/dataset_lister.pl?p=41. Additional data will be uploaded to an online repository on manuscript acceptance.

Author contribution

JAN and MPL conceived the study. JAN, GKL, JPH, GS, CGF, and MPL collected samples and made measurements in the field. JAN, GKL, and GS analyzed samples in the lab. JAN analyzed data and wrote the original paper with supervision by MPL. All authors contributed to data interpretation, review, and editing.

Competing interests

The authors declare that they have no conflict of interest.

Acknowledgements

The NASA Delta-X project is funded by the Science Mission Directorate's Earth Science Division through the Earth Venture Suborbital-3 Program NNH17ZDA001N-EVS3. JAN acknowledges funding from NASA FINESST Grant 80NSSC20K1645. The authors thank Mathieu Dellinger and Amanda Hayton for conducting the ion chromatography at Durham University. We thank Sijia Dong for measuring DIC concentrations. We thank Claire Bucholz, Youli Li, Juliet Ryan-Davis, and Miguel Zepeda-Rosales for assistance with XRF analysis. We thank John Bourg, Madison Douglas, Paola Passalacqua, Eric Prokocki, Maryn Sanders, Adam Songy, and Kyle Wright for field assistance in the Delta-X field campaigns. We also thank participants in Caltech's fall 2019 Ge 121a class for field support in the 2019 field campaign.

References

Agrawal, Y. C. and Pottsmith, H. C.: Instruments for particle size and settling velocity observations in sediment transport, Marine Geology, 168, 89–114, https://doi.org/10.1016/S0025-3227(00)00044-X, 2000.

Benson, T. and French, J. R.: InSiPID: A new low-cost instrument for in situ particle size measurements in estuarine and coastal waters, Journal of Sea Research, 58, 167–188, https://doi.org/10.1016/j.seares.2007.04.003, 2007.

Bevington, A. E., Twilley, R. R., Sasser, C. E., and Holm Jr, G. O.: Contribution of river floods, hurricanes, and cold fronts to elevation change in a deltaic floodplain, northern Gulf of Mexico, USA, Estuarine, Coastal and Shelf Science, 191, 188–200, https://doi.org/10.1016/j.ecss.2017.04.010, 2017.

Blair, N. E. and Aller, R. C.: The Fate of Terrestrial Organic Carbon in the Marine Environment, Annual Review of Marine Science, 4, 401–423, https://doi.org/10.1146/annurev-marine-120709-142717, 2012.

Blum, M. D. and Roberts, H. H.: Drowning of the Mississippi Delta due to insufficient sediment supply and global sea-level rise, Nature Geoscience, 2, 488–491, https://doi.org/10.1038/NGEO55, 2009.

Bouchez, J., Galy, V., Hilton, R. G., Gaillardet, J., Moreira-Turcq, P., Pérez, M. A., France-Lanord, C., and Maurice, L.: Source, transport and fluxes of Amazon River particulate organic carbon: Insights from river sediment depth-profiles, Geochimica et Cosmochimica Acta, 133, 280–298, https://doi.org/10.1016/j.gca.2014.02.032, 2014.

Braat, L., van Kessel, T., Leuven, J. R., and Kleinhans, M. G.: Effects of mud supply on large-scale estuary morphology and development over centuries to millennia, Earth Surface Dynamics, 5, 617–652, https://doi.org/10.5194/esurf-5-617-2017, 2017.

Brinkman, H. C.: A calculation of the viscous force exerted by a flowing fluid on a dense swarm of particles, Applied Scientific Research, A1, 27–34, https://doi.org/10.1007/BF02120313, 1947.

Bushell, G. and Amal, R.: Fractal aggregates of polydisperse particles, Journal of colloid and interface science, 205, 459–469, https://doi.org/10.1006/jcis.1998.5667, 1998.

Bushell, G. and Amal, R.: Measurement of fractal aggregates of polydisperse particles using small-angle light scattering, Journal of colloid and interface science, 221, 186–194, https://doi.org/10.1006/jcis.1999.6532, 2000.

Carstens, M. R.: Accelerated motion of a spherical particle, Eos, Transactions American Geophysical Union, 33, 713–721, https://doi.org/10.1029/TR033i005p00713, 1952.

Chase, R. R.: Settling behavior of natural aquatic particulates, Limnology and Oceanography, 24, 417–426, https://doi.org/10.4319/lo.1979.24.3.0417, 1979.

Cohen, S., Syvitski, J., Ashley, T., Lammers, R., Fekete, B., and Li, H.-Y.: Spatial trends and drivers of bedload and suspended sediment fluxes in global rivers, Water Resources Research, 58, e2021WR031583, https://doi.org/10.1029/2021WR031583, 2022.

Csanady, G. T.: Turbulent diffusion of heavy particles in the atmosphere, Journal of Atmospheric Sciences, 20, 201–208, https://doi.org/10.1175/1520-0469(1963)020%3C0201:TDOHPI%3E2.0.CO;2, 1963.

Davies, C. N.: The separation of airborne dust and particles, Proceedings of the Institution of mechanical engineers, 167, 185–213, https://doi.org/10.1177/002034835316701b13, 1953.

De Leeuw, J., Lamb, M. P., Parker, G., Moodie, A. J., Haught, D., Venditti, J. G., and Nittrouer, J. A.: Entrainment and suspension of sand and gravel, Earth Surface Dynamics, 8, 485–504, https://doi.org/10.5194/esurf-8-485-2020, 2020.

Dietrich, W. E.: Settling velocity of natural particles, Water Resources Research, 18, 1615–1626, https://doi.org/10.1029/WR018i006p01615, 1982.

Dong, S., Subhas, A. V., Rollins, N. E., Naviaux, J. D., Adkins, J. F., and Berelson, W. M.: A kinetic pressure effect on calcite dissolution in seawater, Geochimica et Cosmochimica Acta, 238, 411–423, https://doi.org/10.1016/j.gca.2018.07.015, 2018.

Douglas, M. M., Li, G. K., Fischer, W. W., Rowland, J. C., Kemeny, P. C., West, A. J., Schwenk, J., Piliouras, A. P., Chadwick, A. J., and Lamb, M. P.: Organic carbon burial by river meandering partially offsets bank-erosion carbon fluxes in a discontinuous permafrost floodplain, Earth Surface Dynamics Discussions, 10, 1–24, https://doi.org/10.5194/esurf-10-421-2022, 2022.

Droppo, I. G. and Ongley, E. D.: Flocculation of suspended sediment in rivers of southeastern Canada, Water Research, 28, 1799–1809, https://doi.org/10.1016/0043-1354(94)90253-4, 1994.

Dyer, K. R. and Manning, A. J.: Observation of the size, settling velocity and effective density of flocs, and their fractal 1000 dimensions, Journal of sea research, 41, 87–95, https://doi.org/10.1016/S1385-1101(98)00036-7, 1999.

Edwards, T. K. and Glysson, G. D.: Field methods for measurement of fluvial sediment, US Geological Survey Denver, CO, 1999.

Egan, G., Chang, G., Manning, A. J., Monismith, S., and Fringer, O.: On the variability of floc characteristics in a shallow estuary, Journal of Geophysical Research: Oceans, 127, e2021JC018343, https://doi.org/10.1029/2021JC018343, 2022.

1005 Eisma, D., Cadée, G. C., Laane, R., and Kalf, J.: Preliminary results of AURELIA-and NAVICULA Cruises in the Rhine- and Ems-estuaries, January-February, 1982, Mitteilungen aus dem Geologisch-Paläontologischen Institut der Universität Hamburg, 633–654, 1982.

Ferguson, R. I. and Church, M.: A Simple Universal Equation for Grain Settling Velocity, Journal of Sedimentary Research, 74, 933–937, https://doi.org/10.1306/051204740933, 2004.

1010 Fichot, C. and Harringmeyer, J.: Delta-X: In situ Beam Attenuation and Particle Size from LISST-200X, 2021, ORNL DAAC, https://doi.org/10.3334/ORNLDAAC/2077, 2021.

Galy, V., France-Lanord, C., and Lartiges, B.: Loading and fate of particulate organic carbon from the Himalaya to the Ganga–Brahmaputra delta, Geochimica et Cosmochimica Acta, 72, 1767–1787, https://doi.org/10.1016/j.gca.2008.01.027, 2008.

1015 García, M. H.: Sediment Transport and Morphodynamics, Sedimentation Engineering: Processes, Measurements, Modeling, and Practice, 21–163, https://doi.org/10.1061/9780784408148.ch02, 2008.

Geider, R. J., Delucia, E. H., Falkowski, P. G., Finzi, A. C., Grime, J. P., Grace, J., Kana, T. M., La Roche, J., Long, S. P., and Osborne, B. A.: Primary productivity of planet earth: biological determinants and physical constraints in terrestrial and aquatic habitats, Global Change Biology, 7, 849–882, https://doi.org/10.1046/j.1365-2486.2001.00448.x, 2001.

1020 Geleynse, N., Hiatt, M., Sangireddy, H., and Passalacqua, P.: Identifying environmental controls on the shoreline of a natural river delta, Journal of Geophysical Research: Earth Surface, 120, 877–893, https://doi.org/10.1002/2014JF003408, 2015.

Gibbs, R. J.: Estuarine flocs: their size, settling velocity and density, Journal of Geophysical Research: Oceans, 90, 3249–3251, https://doi.org/10.1029/JC090iC02p03249, 1985.

Gmachowski, L.: Mass–radius relation for fractal aggregates of polydisperse particles, Colloids and Surfaces A: 1025 Physicochemical and Engineering Aspects, 224, 45–52, https://doi.org/10.1016/S0927-7757(03)00318-2, 2003.

Graf, W. H. and Cellino, M.: Suspension flows in open channels; experimental study, Journal of Hydraulic Research, 40, 435–447, https://doi.org/10.1080/00221680209499886, 2002.

Graham, G. W. and Nimmo Smith, W. A. M.: The application of holography to the analysis of size and settling velocity of suspended cohesive sediments, Limnology and Oceanography: Methods, 8, 1–15, https://doi.org/10.4319/lom.2010.8.1, 1030 2010.

Graham, G. W., Davies, E. J., Nimmo-Smith, W. A. M., Bowers, D. G., and Braithwaite, K. M.: Interpreting LISST-100X measurements of particles with complex shape using digital in-line holography, Journal of Geophysical Research: Oceans, 117, https://doi.org/10.1029/2011JC007613, 2012.

Guo, L. and He, Q.: Freshwater flocculation of suspended sediments in the Yangtze River, China, Ocean Dynamics, 61, 371–386, https://doi.org/10.1007/s10236-011-0391-x, 2011.

Hill, P. S., Milligan, T. G., and Geyer, W. R.: Controls on effective settling velocity of suspended sediment in the Eel River flood plume, Continental Shelf Research, 20, 2095–2111, https://doi.org/10.1016/S0278-4343(00)00064-9, 2000.

Hill, P. S., Voulgaris, G., and Trowbridge, J. H.: Controls on floc size in a continental shelf bottom boundary layer, Journal of Geophysical Research: Oceans, 106, 9543–9549, https://doi.org/10.1029/2000JC900102, 2001.

Izquierdo–Ayala, K., Garcia–Aragon, J. A., Castillo–Uzcanga, M. M., and Salinas-Tapia, H.: Freshwater flocculation dependence on turbulence properties in the Usumacinta river, Journal of Hydraulic Engineering, 147, 05021009, https://doi.org/10.1061/(ASCE)HY.1943-7900.0001940, 2021.

Izquierdo-Ayala, K., García-Aragón, J. A., Castillo-Uzcanga, M. M., Díaz-Delgado, C., Carrillo, L., and Salinas-Tapia, H.: Flocculation Patterns Related to Intra-Annual Hydrodynamics Variability in the Lower Grijalva-Usumacinta System, Water, 15, 292, https://doi.org/10.3390/w15020292, 2023.

Jarvis, P., Jefferson, B., and Parsons, S. A.: Measuring floc structural characteristics, Reviews in Environmental Science and Bio/Technology, 4, 1–18, https://doi.org/10.1007/s11157-005-7092-1, 2005.

Jensen, D. J., Cavanaugh, K. C., Thompson, D. R., Fagherazzi, S., Cortese, L., and Simard, M.: Leveraging the historical Landsat catalog for a remote sensing model of wetland accretion in coastal Louisiana, Journal of Geophysical Research: Biogeosciences, 127, e2022JG006794, https://doi.org/10.1029/2022JG006794, 2022.

Johnson, C. P., Li, X., and Logan, B. E.: Settling velocities of fractal aggregates, Environmental science & technology, 30, 1911–1918, https://doi.org/10.1021/es950604g, 1996.

Keyvani, A. and Strom, K.: A fully-automated image processing technique to improve measurement of suspended particles and flocs by removing out-of-focus objects, Computers & Geosciences, 52, 189–198, https://doi.org/10.1016/j.cageo.2012.08.018, 2013.

Khelifa, A. and Hill, P. S.: Models for effective density and settling velocity of flocs, Journal of Hydraulic Research, 44, 390–401, https://doi.org/10.1080/00221686.2006.9521690, 2006.

Kim, A. S. and Stolzenbach, K. D.: The permeability of synthetic fractal aggregates with realistic three-dimensional structure, Journal of colloid and interface science, 253, 315–328, https://doi.org/10.1006/jcis.2002.8525, 2002.

Kranck, K.: The role of flocculation in the filtering of particulate matter in estuaries, The estuary as a filter, 159–175, https://doi.org/10.1016/B978-0-12-405070-9.50014-1, 1984.

Kranck, K. and Milligan, T.: Macroflocs: production of marine snow in the laboratory, Marine Ecology - Progress Series, 3, 19–24, 1980.

Kranenburg, C.: The fractal structure of cohesive sediment aggregates, Estuarine, Coastal and Shelf Science, 39, 451–460, https://doi.org/10.1016/S0272-7714(06)80002-8, 1994.

1065

Krishnappan, B. G.: In situ size distribution of suspended particles in the Fraser River, Journal of Hydraulic Engineering, 126, 561–569, https://doi.org/10.1061/(ASCE)0733-9429(2000)126:8(561), 2000.

Kumar, R. G., Strom, K. B., and Keyvani, A.: Floc properties and settling velocity of San Jacinto estuary mud under variable shear and salinity conditions, Continental Shelf Research, 30, 2067–2081, https://doi.org/10.1016/j.csr.2010.10.006, 2010.

1070 Kuprenas, R., Tran, D., and Strom, K.: A Shear-Limited Flocculation Model for Dynamically Predicting Average Floc Size, Journal of Geophysical Research: Oceans, 123, 6736–6752, https://doi.org/10.1029/2018JC014154, 2018.

Lamb, M. P., De Leeuw, J., Fischer, W. W., Moodie, A. J., Venditti, J. G., Nittrouer, J. A., Haught, D., and Parker, G.: Mud in rivers transported as flocculated and suspended bed material, Nature Geoscience, 13, 566–570, https://doi.org/10.1038/s41561-020-0602-5, 2020.

1075 Larsen, L. G., Harvey, J. W., and Crimaldi, J. P.: Morphologic and transport properties of natural organic floc, Water Resources Research, 45, https://doi.org/10.1029/2008WR006990, 2009.

Latimer, R. A. and Schweizer, C. W.: The Atchafalaya River Study: a report based upon engineering and geological studies of the enlargement of Old and Atchafalaya Rivers, 1951.

Lee, B. J., Kim, J., Hur, J., Choi, I. H., Toorman, E. A., Fettweis, M., and Choi, J. W.: Seasonal Dynamics of Organic Matter 1080 Composition and Its Effects on Suspended Sediment Flocculation in River Water, Water Resources Research, 55, 6968–6985, https://doi.org/10.1029/2018WR024486, 2019.

Li, X. and Logan, B. E.: Collision frequencies of fractal aggregates with small particles by differential sedimentation, Environmental science & technology, 31, 1229–1236, https://doi.org/10.1021/es960771w, 1997.

Li, X.-Y. and Logan, B. E.: Permeability of fractal aggregates, Water research, 35, 3373–3380, 1085 https://doi.org/10.1016/S0043-1354(01)00061-6, 2001.

Maggi, F., Mietta, F., and Winterwerp, J. C.: Effect of variable fractal dimension on the floc size distribution of suspended cohesive sediment, Journal of Hydrology, 343, 43–55, https://doi.org/10.1016/j.jhydrol.2007.05.035, 2007.

Matsuo, T. and Unno, H.: Forces acting on floc and strength of floc, Journal of the Environmental Engineering Division, 107, 527–545, https://doi.org/10.1061/JEEGAV.0001174, 1981.

1090 Mayer, L. M.: Surface area control of organic carbon accumulation in continental shelf sediments, Geochimica et Cosmochimica Acta, 58, 1271–1284, https://doi.org/10.1016/0016-7037(94)90381-6, 1994.

McCave, I. N.: Size spectra and aggregation of suspended particles in the deep ocean, Deep Sea Research Part A. Oceanographic Research Papers, 31, 329–352, https://doi.org/10.1016/0198-0149(84)90088-8, 1984.

McNown, J. S. and Malaika, J.: Effects of particle shape on settling velocity at low Reynolds numbers, Eos, Transactions 1095 American Geophysical Union, 31, 74–82, https://doi.org/10.1029/TR031i001p00074, 1950.

Mikkelsen, O. and Pejrup, M.: The use of a LISST-100 laser particle sizer for in-situ estimates of floc size, density and settling velocity, Geo-Marine Letters, 20, 187–195, https://doi.org/10.1007/s003670100064, 2001.

Mikkelsen, O. A., Milligan, T. G., Hill, P. S., and Moffatt, D.: INSSECT—an instrumented platform for investigating floc properties close to the seabed, Limnology and Oceanography: Methods, 2, 226–236, https://doi.org/10.4319/lom.2004.2.226, 2004.

Mikkelsen, O. A., Hill, P. S., Milligan, T. G., and Chant, R. J.: In situ particle size distributions and volume concentrations from a LISST-100 laser particle sizer and a digital floc camera, Continental Shelf Research, 25, 1959–1978, https://doi.org/10.1016/j.csr.2005.07.001, 2005.

Mikkelsen, O. A., Hill, P. S., and Milligan, T. G.: Seasonal and spatial variation of floc size, settling velocity, and density on the inner Adriatic Shelf (Italy), Continental Shelf Research, 27, 417–430, https://doi.org/10.1016/j.csr.2006.11.004, 2007.

Moodie, A. J., Nittrouer, J. A., Ma, H., Carlson, B. N., Wang, Y., Lamb, M. P., and Parker, G.: Suspended-sediment induced stratification inferred from concentration and velocity profile measurements in the lower Yellow River, China, Water Resources Research, e2020WR027192, https://doi.org/10.1029/2020WR027192, 2020.

Neale, G., Epstein, N., and Nader, W.: Creeping flow relative to permeable spheres, Chemical Engineering Science, 28, 1865–1874, https://doi.org/10.1016/0009-2509(73)85070-5, 1973.

Nelson, C. H. and Lamothe, P. J.: Heavy metal anomalies in the Tinto and Odiel river and estuary system, Spain, Estuaries, 16, 496–511, https://doi.org/10.2307/1352597, 1993.

Nezu, I. and Nakagawa, H.: Turbulence in open-channel flows, AA Balkema, Rotterdam, 1–281, 1993.

Nghiem, J., Salter, G., and Lamb, M. P.: Delta-X: Bed and Suspended Sediment Grain Size, MRD, LA, USA, 2021, Version 2, ORNL DAAC, https://doi.org/10.3334/ORNLDAAC/2135, 2021.

Nghiem, J. A., Fischer, W. W., Li, G. K., and Lamb, M. P.: A Mechanistic Model for Mud Flocculation in Freshwater Rivers, Journal of Geophysical Research: Earth Surface, e2021JF006392, https://doi.org/10.1029/2021JF006392, 2022.

Nicholas, A. P. and Walling, D. E.: The significance of particle aggregation in the overbank deposition of suspended sediment on river floodplains, Journal of Hydrology, 186, 275–293, https://doi.org/10.1016/S0022-1694(96)03023-5, 1996.

Osborn, R., Dillon, B., Tran, D., Abolfazli, E., Dunne, K. B., Nittrouer, J. A., and Strom, K.: FlocARAZI: an in-situ, image-based profiling instrument for sizing solid and flocculated suspended sediment, Journal of Geophysical Research: Earth Surface, e2021JF006210, https://doi.org/10.1029/2021JF006210, 2021.

Osborn, R., Dunne, K. B., Ashley, T., Nittrouer, J. A., and Strom, K.: The flocculation state of mud in the lowermost freshwater reaches of the Mississippi River: spatial distribution of sizes, seasonal changes, and their impact on vertical concentration profiles, Journal of Geophysical Research: Earth Surface, e2022JF006975, https://doi.org/10.1029/2022JF006975, 2023.

Phillips, C. B., Masteller, C. C., Slater, L. J., Dunne, K. B., Francalanci, S., Lanzoni, S., Merritts, D. J., Lajeunesse, E., and Jerolmack, D. J.: Threshold constraints on the size, shape and stability of alluvial rivers, Nature Reviews Earth & Environment, 3, 406–419, https://doi.org/10.1038/s43017-022-00282-z, 2022.

Pizzuto, J. E.: Long-term storage and transport length scale of fine sediment: Analysis of a mercury release into a river, Geophysical Research Letters, 41, 5875–5882, https://doi.org/10.1002/2014GL060722, 2014.

Roberts, H. H., Adams, R. D., and Cunningham, R. H. W.: Evolution of sand-dominant subaerial phase, Atchafalaya Delta, Louisiana, AAPG Bulletin, 64, 264–279, https://doi.org/10.1306/2F918964-16CE-11D7-8645000102C1865D, 1980.

Roberts, W., Le Hir, P., and Whitehouse, R. J. S.: Investigation using simple mathematical models of the effect of tidal currents and waves on the profile shape of intertidal mudflats, Continental Shelf Research, 20, 1079–1097, https://doi.org/10.1016/S0278-4343(00)00013-3, 2000.

Rommelfanger, N., Vowinckel, B., Wang, Z., Dohrmann, R., Meiburg, E., and Luzzatto-Fegiz, P.: A simple criterion and experiments for onset of flocculation in kaolin clay suspensions, arXiv preprint arXiv:2203.15545, https://doi.org/10.48550/arXiv.2203.15545, 2022.

Rouse, H.: Modern conceptions of the mechanics of fluid turbulence, Transactions of the American Society of Civil Engineers, 102, 463–505, https://doi.org/10.1061/TACEAT.0004872, 1937.

Sequoia Scientific: LISST-200X Particle Size Analyzer User's Manual, 2022.

Shen, X., Lee, B. J., Fettweis, M., and Toorman, E. A.: A tri-modal flocculation model coupled with TELEMAC for estuarine muds both in the laboratory and in the field, Water research, 145, 473–486, https://doi.org/10.1016/j.watres.2018.08.062, 2018.

Smellie, R. H. and La Mer, V. K.: Flocculation, subsidence and filtration of phosphate slimes: VI. A quantitative theory of filtration of flocculated suspensions, Journal of Colloid Science, 13, 589–599, https://doi.org/10.1016/0095-8522(58)90071-0, 1958.

Smith, S. J. and Friedrichs, C. T.: Size and settling velocities of cohesive flocs and suspended sediment aggregates in a trailing suction hopper dredge plume, Continental Shelf Research, 31, S50–S63, https://doi.org/10.1016/j.csr.2010.04.002, 2011.

Son, M. and Hsu, T.-J.: The effects of flocculation and bed erodibility on modeling cohesive sediment resuspension, Journal of Geophysical Research: Oceans, 116, https://doi.org/10.1029/2010JC006352, 2011.

Stokes, G. G.: On the effect of the internal friction of fluids on the motion of pendulums, Transactions of the Cambridge Philosophical Society, 1851.

Strom, K. and Keyvani, A.: An explicit full-range settling velocity equation for mud flocs, Journal of Sedimentary Research, 81, 921–934, https://doi.org/10.2110/jsr.2011.62, 2011.

Syvitski, J. P., Asprey, K. W., and Leblanc, K. W. G.: In-situ characteristics of particles settling within a deep-water estuary, Deep Sea Research Part II: Topical Studies in Oceanography, 42, 223–256, https://doi.org/10.1016/0967-0645(95)00013-G, 1995.

Syvitski, J. P., Kettner, A. J., Overeem, I., Hutton, E. W., Hannon, M. T., Brakenridge, G. R., Day, J., Vörösmarty, C., Saito, Y., and Giosan, L.: Sinking deltas due to human activities, Nature Geoscience, 2, 681–686, https://doi.org/10.1038/ngeo629, 2009.

Tambo, N. and Watanabe, Y.: Physical characteristics of flocs—I. The floc density function and aluminium floc, Water Research, 13, 409–419, https://doi.org/10.1016/0043-1354(79)90033-2, 1979.

Tennekes, H. and Lumley, J. L.: A first course in turbulence, MIT Press, 1972.

Tran, D., Kuprenas, R., and Strom, K.: How do changes in suspended sediment concentration alone influence the size of mud flocs under steady turbulent shearing?, Continental Shelf Research, 158, 1–14, https://doi.org/10.1016/j.csr.2018.02.008, 2018.

1170 Van Leussen, W.: Aggregation of Particles, Settling Velocity of Mud Flocs A Review, in: Physical Processes in Estuaries, Berlin, Heidelberg, 347–403, https://doi.org/10.1007/978-3-642-73691-9_19, 1988.

Van Rijn, L. C.: Sediment Transport, Part II: Suspended Load Transport, Journal of Hydraulic Engineering, 110, 1613–1641, https://doi.org/10.1061/(ASCE)0733-9429(1984)110:11(1613), 1984.

Walling, D. E. and Fang, D.: Recent trends in the suspended sediment loads of the world's rivers, Global and planetary
1175 change, 39, 111–126, https://doi.org/10.1016/S0921-8181(03)00020-1, 2003.

West, A. J., Galy, A., and Bickle, M.: Tectonic and climatic controls on silicate weathering, Earth and Planetary Science Letters, 235, 211–228, https://doi.org/10.1016/j.epsl.2005.03.020, 2005.

Winterwerp, J. C.: A simple model for turbulence induced flocculation of cohesive sediment, Journal of Hydraulic Research, 36, 309–326, https://doi.org/10.1080/00221689809498621, 1998.

1180 Woodfield, D. and Bickert, G.: An improved permeability model for fractal aggregates settling in creeping flow, Water research, 35, 3801–3806, https://doi.org/10.1016/S0043-1354(01)00128-2, 2001.

Wright, S. and Parker, G.: Density stratification effects in sand-bed rivers, Journal of Hydraulic Engineering, 130, 783–795, https://doi.org/10.1061/(ASCE)0733-9429(2004)130:8(783), 2004.

Xu, F., Wang, D.-P., and Riemer, N.: Modeling flocculation processes of fine-grained particles using a size-resolved
1185 method: comparison with published laboratory experiments, Continental Shelf Research, 28, 2668–2677, https://doi.org/10.1016/j.csr.2008.09.001, 2008.

Zeichner, S. S., Nghiem, J., Lamb, M. P., Takashima, N., De Leeuw, J., Ganti, V., and Fischer, W. W.: Early plant organics increased global terrestrial mud deposition through enhanced flocculation, Science, 371, 526–529, https://doi.org/10.1126/science.abd0379, 2021.

1190